

# Fracture sealing and its impact on the percolation of subsurface fracture networks

Weiwei Zhu<sup>1</sup>, Xupeng He<sup>1</sup>, Siarhei Khirevich<sup>1</sup>, Tad W. Patzek<sup>1</sup>

<sup>1</sup>Ali I. Al-Naimi Petroleum Engineering Research Center (ANPERC), King Abdullah University of Science and Technology, Thuwal, KSA.

## Key Points:

- We simulate the impact of sealing on the percolation in two- and three-dimensional fracture networks.
- We find that partially sealed, conductive fractures form locally connected clusters.
- We estimate the stimulated reservoir volume in a simple but physically meaningful way.

---

Corresponding author: Weiwei Zhu, [weiwei.zhu@kaust.edu.sa](mailto:weiwei.zhu@kaust.edu.sa)

## Abstract

Fractures play an essential role in formations with low permeability; however, fracture sealing significantly reduces the permeability of fractures. The mechanism of how fracture sealing impacts the macro-scale fluid flow is rarely investigated. Here, we simulate sealing in two- and three-dimensional orthogonal fracture networks and investigate the impact of sealing on the percolation of these fracture networks. We find that a small amount of sealing can prevent the formation of spanning clusters, which suggests that global connectivity is rarely realized. Without significant stress perturbations, most fractures are partially sealed and non-critically stressed, and they usually do not contribute much to the fluid flow. However, under a significant stress perturbation, such as hydraulic fracturing, the well-connected and critically oriented fractures become critically stressed and slide because of the increased pore pressure. Partially sealed and non-critically stressed fractures can also contribute to the fluid flow by enlarging the stimulated reservoir volume (SRV). We estimate the stimulated reservoir volume in two dimensions by dividing the target distance ( $L_{SRV}$ ) into two parts. One is the distance limiting generation of hydraulic fractures ( $\Delta L_h$ ), and the other is the limiting distance of making natural fractures slide ( $\Delta L_s$ ). A rough estimation yields an elongated shape of the SRV, which is consistent with observations from microseismicity maps.

## Plain Language Summary

Fractures are regarded as high-permeable pathways for any fluid flow in the subsurface. However, the fracture closing and sealing can significantly reduce the fracture's permeability. To evaluate the impact of fracture sealing on the hydraulic conductivity of complex fracture networks is nontrivial because of the enormous scale difference between these two phenomena. Fracture sealing usually happens at the scale of micrometers or millimeters, while fractures vary in size from micrometers to kilometers. In this research, we simulate sealing in two- and three-dimensional orthogonal fracture networks with in-house software and investigate the impact of sealing on the formation of a spanning cluster in complex fracture networks. We find that a small amount of sealing can prevent the formation of a spanning cluster. Partially sealed natural fractures form locally connected, open clusters. However, with hydraulic fracturing, where the pore pressure increases significantly, critically stressed fractures are reactivated and create high-permeable pathways (stimulated reservoir volume) for fluid flow. Non-critically stressed and partially sealed fractures can also enlarge SRV and contribute to production. Therefore, a geometrically well-connected fracture network cannot ensure good hydraulic conductivity. We have to consider the current stress states and their sealing patterns for a more comprehensive evaluation.

## 1 Introduction

Brittle rocks in the Earth's upper crust are ubiquitously fractured. In many engineering fields, such as hydrology, waste disposal, geothermal and petroleum reservoir exploitation (Berkowitz, 2002), fractures play an essential role. Most fractures are permeable immediately after their formation, and they provide dominant pathways for fluid flows in low permeability formations. However, over geologic time, compression and cementation can cause the closure and sealing of fractures, which together significantly reduce the fracture permeabilities (Im et al., 2018; Ito & Zoback, 2000).

Hubbert et al. (1956); Hubbert and Willis (1972) and C. A. Barton et al. (1995) proposed a critically stressed fault hypothesis, and argued that hydrologically conductive faults are critically stressed in today's stress field. In critically stressed fractures, the ratio of shear to normal stresses exceeds the frictional strength of the rock. The Coulomb failure criterion (Coulomb, 1773) was found to be appropriate in describing frictional sliding of fractures (Im et al., 2018; Mattila & Follin, 2019; Evans, 2005):

$$\tau = \mu(S_n - P_p), \quad (1)$$

where  $\mu$  is the coefficient of friction along the fracture plane,  $P_p$  is local pore pressure, and  $\tau$  and  $S_n$  are respectively shear and normal stresses on a fracture. To demonstrate the concept of critically stressed fractures, a three-dimensional (3D) fracture network is constructed in Fig. 1 and the stress state of each fracture plane is shown in the Mohr diagram. The orientations of fractures are uniform, because subsurface rocks may have many different sets of fractures formed during their geologic history (C. A. Barton et al., 1995). In Fig. 1,  $S_2$  is the reference stress, with  $S_1 = 1.3S_2$ ,  $S_3 = 0.6S_2$  and  $P_p = 0.5S_2$ . The Coulomb failure

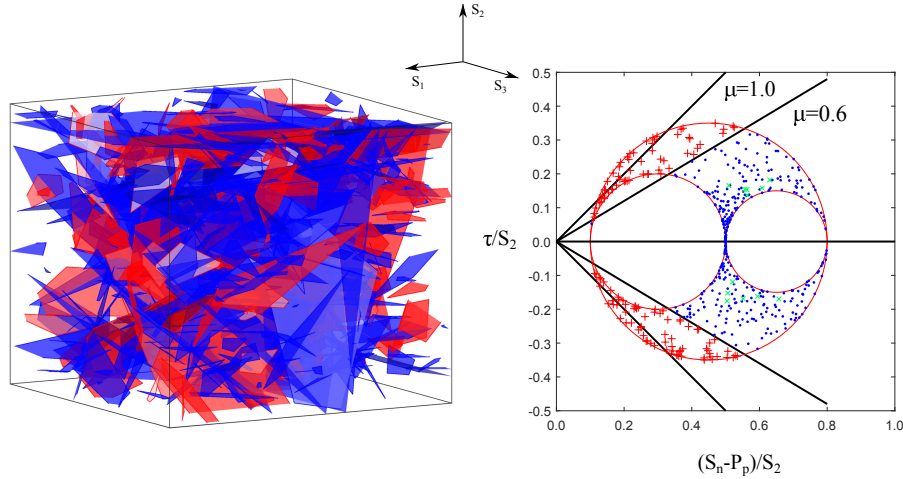


**Figure 1.** Left: a 3D fracture network composed of critically (red polygons) and non-critically (blue polygons) stressed fractures. Right: normalized shear *vs.* effective normal stress for critically (red pluses) and non-critically (blue dots) stressed fractures. The green crosses indicate hydraulically conductive fractures with their stress mapping points far away from the failure line. The failure lines are shown for a Coulomb friction criterion with the friction coefficients of 0.6 and 1.0.

criterion is imperfect since it cannot quantify impacts of a natural fracture surface, such as roughness and compressive strength, but it is simple and widely used in many engineering fields. It is good enough to implement the Coulomb criterion as the first attempt. Detailed investigations of a shear failure criterion that involves more complex and realistic scenarios are not covered in this research but will be performed in the future. Furthermore, local stress perturbations induced by interactions of neighbouring fractures are also neglected, because i. fractures usually need to be close enough to have a significant stress perturbation (Thomas et al., 2017); ii. numerical calculations of stress fields are expensive in complex discrete fracture networks with thousands of realizations.

Sliding of critically stressed fractures induces shear displacement and enlarges the fracture aperture because of roughness (Yeo et al., 1998; Kim & Inoue, 2003; Wenning et al., 2019; Frash et al., 2019). Identifying the critically stressed fractures is essential because they are highly permeable and significantly contribute to fluid flow (C. A. Barton et al., 1995; Ito & Zoback, 2000; Xie & Min, 2016; Ito & Hayashi, 2003). However, the number of critically stressed fractures can vary widely, because this number strongly depends on the global and local stress state, fracture orientations and the frictional strength of the rock. Non-critically stressed fractures are usually sealed and irrelevant to flow considerations. However, fractures are usually only partially sealed, not completely sealed. The complex

process of crystal growth can result in different sealing patterns, such as massive sealing deposits, thin rinds or veneers that line the surfaces of open fractures, and bridge structures that span otherwise open fractures (Lander & Laubach, 2015; S. Laubach, Reed, et al., 2004). How exactly fracture sealing prevents macro-scale hydraulic responses is rarely investigated. However, there are exceptions. C. A. Barton et al. (1995) and Ito and Zoback (2000) observed some hydraulically conductive fractures with their stress mapping points far away from the failure line in the Mohr diagram (see the green crosses in Fig. 1). The fracture strength can be weakened by the presence of weak minerals, such as graphite, kaolinite, chrysotile and illite (Morrow et al., 2000); however, this may not explain their observations because similar exceptions exist in strong rocks, and the stress mapping points can be far away from the failure line. These observations lead us to ask the following questions:

1. Why the non-critically stressed fractures are usually nonconductive if they are only partially sealed?
2. What are the possible reasons for the green crosses shown in Fig. 1?
3. If non-critically stressed fractures are partially sealed, can they contribute to fluid flow in the subsurface?

To answer these questions, we must couple fracture sealing and complex fracture networks to predict how they jointly impact fluid flow. To date, these two phenomena have been investigated extensively as separate topics (S. E. Laubach, 2003; S. Laubach, Reed, et al., 2004; Ukar & Laubach, 2016; Bour & Davy, 1997). Fractures vary in size from micrometers to kilometers (Berkowitz et al., 2000; Bonnet et al., 2001), while fracture sealing usually happens at the scale of millimeters or micrometers. These huge scale differences make the coupling of these two aspects a challenge. Here, we simulate sealing in complex fracture networks and evaluate its impact on the hydraulic connectivity of the system.

Fracture shapes are complex and irregular in reality, because of the anisotropic and heterogeneous characteristics of rocks and the complex geomechanical environment. Natural fractures also have complex rough surfaces (R. Zimmerman et al., 1991). Tortuosity of the flow paths in a fracture and the stress impact on fractures are also crucial to flow in the fractures (Cook et al., 1990). Complex geometric shapes and dynamic evolution of fractures make detailed characterization of fracture networks difficult. The only practical alternative is the discrete fracture network (DFN) modelling method that preserves critical geometries and topological structures. DFN method explicitly represents fractures with simple geometries, such as line segments in two dimensions and disks or polygons in three dimensions (Lei et al., 2017; Zhu et al., 2019; Zhu, Khirevich, & Patzek, 2021). Different stochastic distributions are applied to mimic the geometrical properties of fractures (Bonnet et al., 2001), such as fracture lengths, orientations, and positions of fracture centers. To make discrete fracture networks representative for this investigation, we choose orthogonal fracture networks (Bai et al., 2002; Rawnsley et al., 1992; Ruf et al., 1998) because they are topologically well-connected, geometrically well-constrained, easy to mimic, and commonly observed in reality. The conclusions derived from orthogonal fracture networks can extend to the other, more realistic configurations of fracture networks.

Because this study focuses on hydraulic connectivity of fracture networks, the cumbersome and expensive flow calculations using a full-scale discrete fracture-matrix model are unnecessary (Karimi-Fard et al., 2003; Sandve et al., 2012). Instead, investigating percolation is sufficient to reveal information about the global and local connectivity of fracture networks. Percolation theory (Stauffer & Aharony, 1994) has been used by many researchers to study connectivity of anything in general and connectivity of fractures in particular (Mo et al., 1998; Zhu et al., 2018; Robinson, 1983; Berkowitz, 1995; Berkowitz et al., 2000; Bour & Davy, 1997; Masihi et al., 2007). In percolation theory, a percolation parameter that depends on the type of system and process should be identified. This parameter should give a percolation threshold when a spanning cluster is formed in an infinitely large system. Zhu et al. (2018) found that commonly used quantities, such as total excluded volume and



intersections per fracture, are not proper percolation parameters for complex fracture networks. Therefore, finding an appropriate percolation parameter is still an open issue. This research aims to represent global and local connectivity through the spanning cluster and local clusters.

Fracture sealing caused by cementation is a complex process (S. E. Laubach & Ward, 2006), and it depends on the chemistry of the formation fluids, the fluid pressure and the temperature (Lee & Morse, 1999; Budai et al., 2002; Holland & Urai, 2010). Cements are typically divided into two types, synkinematic and postkinematic, which respectively deposit in parallel or after the fracture opening (Ukar & Laubach, 2016; S. Laubach, Lander, et al., 2004; Becker et al., 2010). The thickness of these cements ranges from micron deposits that line fracture walls to crystalline masses that fill fractures and have a thickness of centimeters or more (S. Laubach, Lander, et al., 2004). The uncertainties arising from this range of thickness strongly limit the determination of the spatial distribution of sealing in a subsurface fracture network. Here, we simplify this problem by assuming that the fracture apertures fully control the sealing. The fracture segments with larger apertures have a lower probability of being sealed, and vice versa (Lander & Laubach, 2015; Ukar & Laubach, 2016).

The remainder of this paper is organized as follows: Section 2 introduces techniques to construct the 2D and 3D orthogonal fracture networks, simulate sealing and implement percolation analysis. Section 3 quantifies percolation probability and relative sizes of local clusters. In Section 4, we try to answer the three questions posed in the Introduction and application of this study to the hydraulic fracturing process.

## 2 Materials and methods

In this section, we discuss the generation of orthogonal fracture networks, simulation of fracture sealing and implementation of percolation analysis in 2D and 3D orthogonal fracture networks.

### 2.1 Generation of a 2D orthogonal fracture network

The orthogonal fracture network in this study is composed of two sets of joints, preexisting systematic joints and cross joints, which typically resemble a “ladder-like” pattern in an outcrop (Bai et al., 2002; Rawnsley et al., 1992; Ruf et al., 1998). Cross-joints abut the preexisting joints at angles near  $90^\circ$  and are limited in length by the intervening distance between the preexisting joints. A sketch of this system is shown in Fig. 2. The median

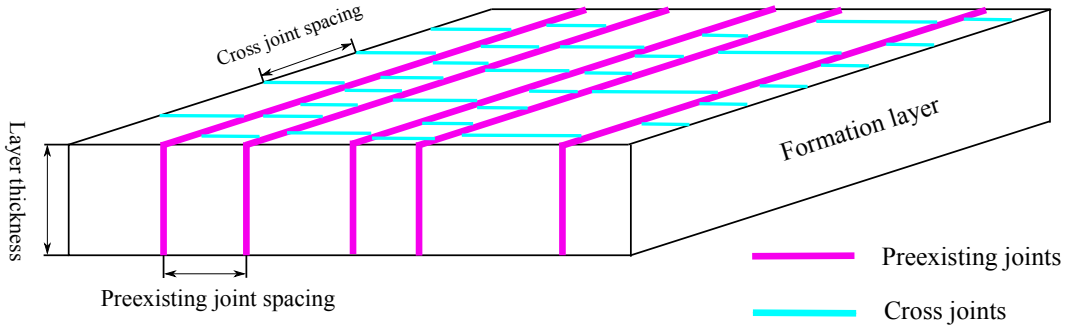


**Figure 2.** Sketch of an orthogonal joint system composed of the preexisting and cross joints.

spacing of the preexisting joints is positively correlated with the formation thickness. It can be quantified as a fracture spacing index (FSI), the slope of the best regression fitting line

in a plot of the mean formation thicknesses *vs.* median joint spacing derived from scanline data. FSI typically varies between 0.7 and 1.5 in most outcrop observations (Bai, Pollard, & Gao, 2000; Gross, 1993; Narr & Suppe, 1991; Engelder et al., 1997; Ruf et al., 1998). Gross (1993) and Bai et al. (2002) found that preexisting joints act as the mechanical layer boundaries for the cross joints, and their spacing functions as a formation thickness. Here, we set the system size as 10 m, the FSI as 1.3 for both the preexisting and cross joint sets and the layer thickness as 0.65 m. The median spacing of the preexisting joints is 0.5 m, correspondingly. The spacing distribution of both fracture sets can follow a negative exponential or log-normal distribution (Sen & Kazi, 1984; Narr & Suppe, 1991). With a negative exponential distribution, the mean and standard deviation are equal, whereas, with a log-normal distribution, the standard deviation of the spacing is typically about 0.56 times the mean spacing (Narr & Suppe, 1991; Huang & Angelier, 1989). A uniform spacing distribution is included as a reference to capture the impact of the spacing distribution on percolation. Fig. 3 shows 2D orthogonal fracture networks with three different spacing distributions for both preexisting and cross joints.

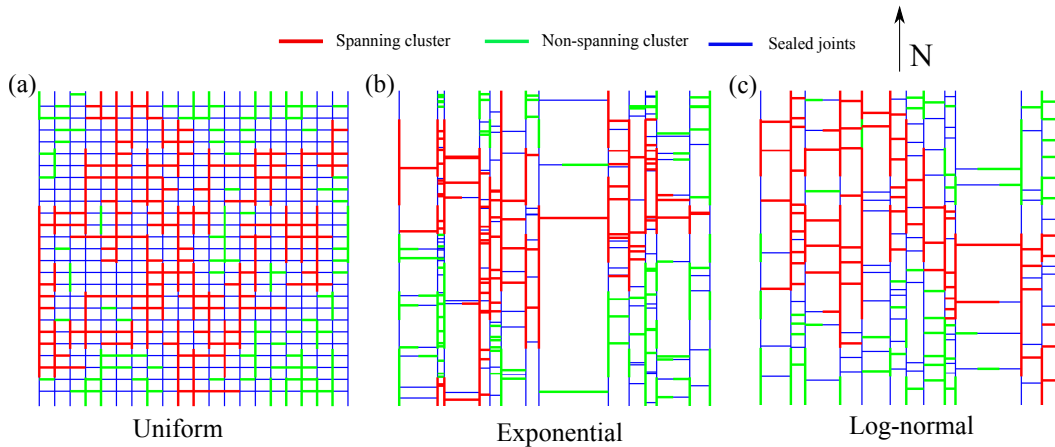


**Figure 3.** 2D orthogonal fracture networks with constant apertures. Preexisting joints have the NS strike, and cross joints have the EW strike; both preexisting and cross joints are spaced according to (a) a uniform distribution; (b) an exponential distribution; (c) a log-normal distribution. The blue line segments indicate sealed fractures; the red line segments are open fractures and form a spanning cluster; the green line segments are open fractures that are locally connected.

## 2.2 Simulation of fracture sealing

Fracture sealing caused by cementation is a complex process that depends on the chemistry of formation fluids, fluid pressure, and temperature. To simplify the problem and mimic the sealing of fractures, we divide each fracture into small segments. Each small segment can be sealed and can block the flow of the fluid. Fig. 4 provides a sketch of the segmentation of a fracture. The small segment can be regarded as the minimum unit of sealing, measured in reality in millimeters or micrometers (S. Laubach, Lander, et al., 2004; S. E. Laubach & Ward, 2006). Each segment has a constant aperture, but segments at different locations in a fracture have different apertures ( $a_i \neq a_j$ ). Simulating the spatial distribution of sealing in a subsurface fracture network is almost impossible to achieve. Here, we simplify the problem by assuming that the sealing of a segment depends only on its aperture. A fracture segment with a larger aperture has a lower probability of being sealed and vice versa. The fracture segment with the largest aperture in the entire fracture network has zero probability of

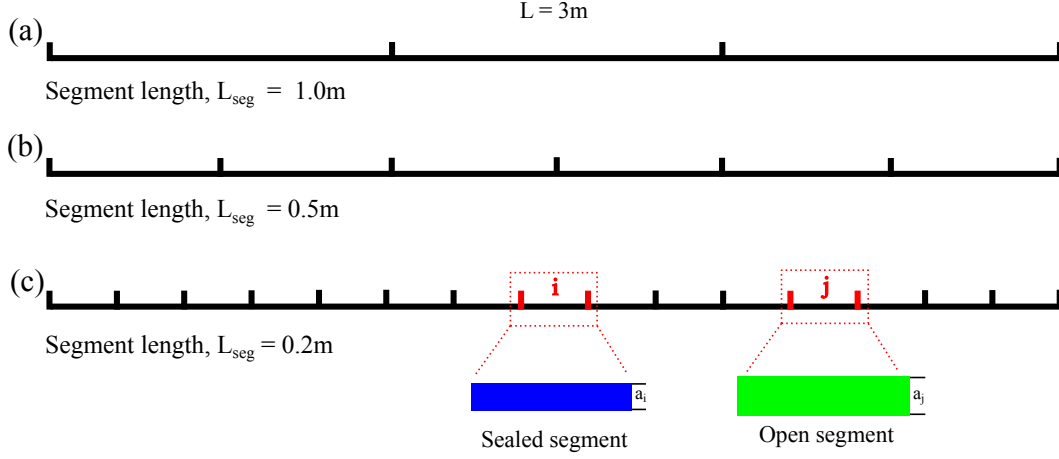


**Figure 4.** Segmentation of 2D fractures. The fracture trace is 3 meter long. (a), (b) and (c) show the segmentation with decreasing segment lengths of 1 m, 0.5 m and 0.2 m, respectively. Each segment has a constant aperture and can be sealed or open, as shown in (c). Segments at different locations have different apertures,  $a_i \neq a_j$ .

being sealed, and the probability of sealing decreases linearly with the aperture size:

$$p_{\text{seal}}^i = 1 - \frac{a_i}{a_{\text{max}}}, \quad (2)$$

where  $p_{\text{seal}}^i$  is the probability of sealing segment *i*;  $a_i$  is the aperture of segment *i*;  $a_{\text{max}}$  is the maximum aperture in the entire fracture network.

The key to finding the spatial distribution of fracture sealing is to determine the aperture size distribution of the fracture segments. We consider three scenarios of aperture distributions sketched in Fig 5:

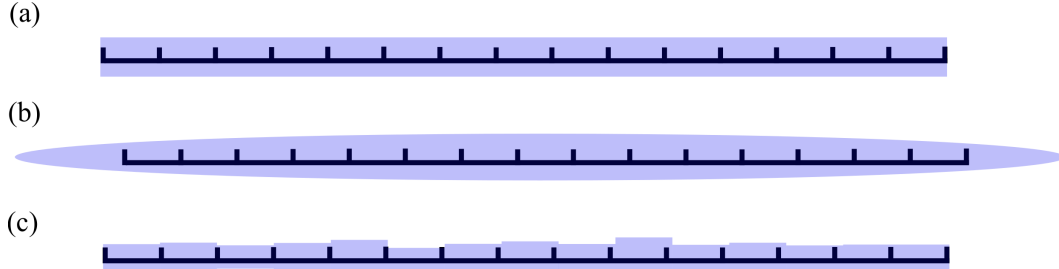


**Figure 5.** Different aperture distributions. The fracture trace is 3 m long, and the segment length  $L_{\text{seg}}$  is 0.2 m. (a) Constant aperture; (b) Elliptical-shaped aperture; (c) Log-normal distributed aperture.

1. Constant aperture;
2. Elliptical-shaped aperture; and
3. Log-normal distributed aperture;

The constant aperture is the simplest but most unrealistic scenario. It serves as a reference to show the impact of aperture distributions on percolation. In this scenario, the

sealing probability of each fracture segment is equal. Sealed segments are shown as blue line segments in Fig. 3, and they have no priority in the spatial distribution.

If linear elastic fracture mechanics (LEFM) is applicable, and if a single fracture in an infinitely large plate is put under remote equibiaxial tensile stress, the shape of the fracture aperture will be elliptical. From the Westergaard stress function method (Westergaard, 1939), the maximum aperture at the fracture center is

$$a_{\text{middle}} = \frac{1 - \nu}{E} \sigma l, \quad (3)$$

where  $a_{\text{middle}}$  is the maximum aperture at the middle of the fracture;  $\nu$  is the Poisson's ratio;  $E$  is the Young's modulus;  $\sigma$  is the magnitude of the equibiaxial tensile stress; and  $l$  is the fracture length. The fracture length is assumed to be 1.2 times the network size to avoid the fracture tips being completely sealed in the fracture network. If we assume  $\nu = 0.25$ ,  $E = 30$  GPa,  $\sigma = 2$  MPa, the maximum aperture at the middle of the fracture will be proportional to the length of the fracture:

$$a_{\text{middle}} = \frac{1}{20,000} l \quad (4)$$

The upper panels in Fig 6 show orthogonal fracture networks with elliptical apertures. Preexisting joints are usually long and have larger apertures; they are thus more likely to be open. Cross joints are usually short and more likely to be sealed. Regions close to fracture tips also have smaller apertures and are subject to more sealing. The spatial distribution of apertures is consistent with many observations from outcrops and core samples (Ukar & Laubach, 2016; Lander & Laubach, 2015).

Log-normal distributed apertures are observed in outcrops and experimental studies (Snow, 1970; R. W. Zimmerman & Bodvarsson, 1996; Muralidharan et al., 2004). The mean value of the aperture is linearly correlated with the fracture length (Bai, Pollard, & Gross, 2000; Olson, 2003). The standard deviation is set to be 0.2 times the mean value, which indicates tortuosity of flow paths in a fracture (Renshaw, 1995). The lower panels in Fig. 6 show the orthogonal fracture networks with the log-normally distributed apertures. The configuration of the fracture networks is similar to the case with elliptical-shaped apertures, where long fractures tend to be open and short ones tend to be sealed.

### 2.3 Percolation analysis

Percolation theory (Stauffer & Aharony, 1994) is used to study connectivity of anything in general (Nomura et al., 2015) and connectivity of fractures in particular (Robinson, 1983; Berkowitz, 1995; Zhu et al., 2018). Classic bond or site percolation problems have a constant probability of opening,  $p$ , for each link or node in the network. For a given probability,  $p$ , the theory captures the probability of forming a spanning cluster. A spanning cluster is an open path connecting the boundaries of the domain. Here, the spanning cluster is composed of intersecting fractures connecting four sides in the 2D fracture network. The fracture network considered here are far more complex than a classic bond percolation problem because i. the system has irregular lattices and changes its configuration for each realization; ii. the probability of opening is not constant but varies with the aperture sizes of fracture segments. Therefore, the classic excluded-volume based percolation parameter is inapplicable. Finding a proper percolation parameter and its threshold, which should depend on specific configurations of fracture networks and be valid in an infinitely large system, is out of the scope of this research. Instead, we aim to represent global and local connectivity with the spanning and local clusters. The probability of forming a spanning cluster with a given fraction of open joints in each fracture network is approximated by

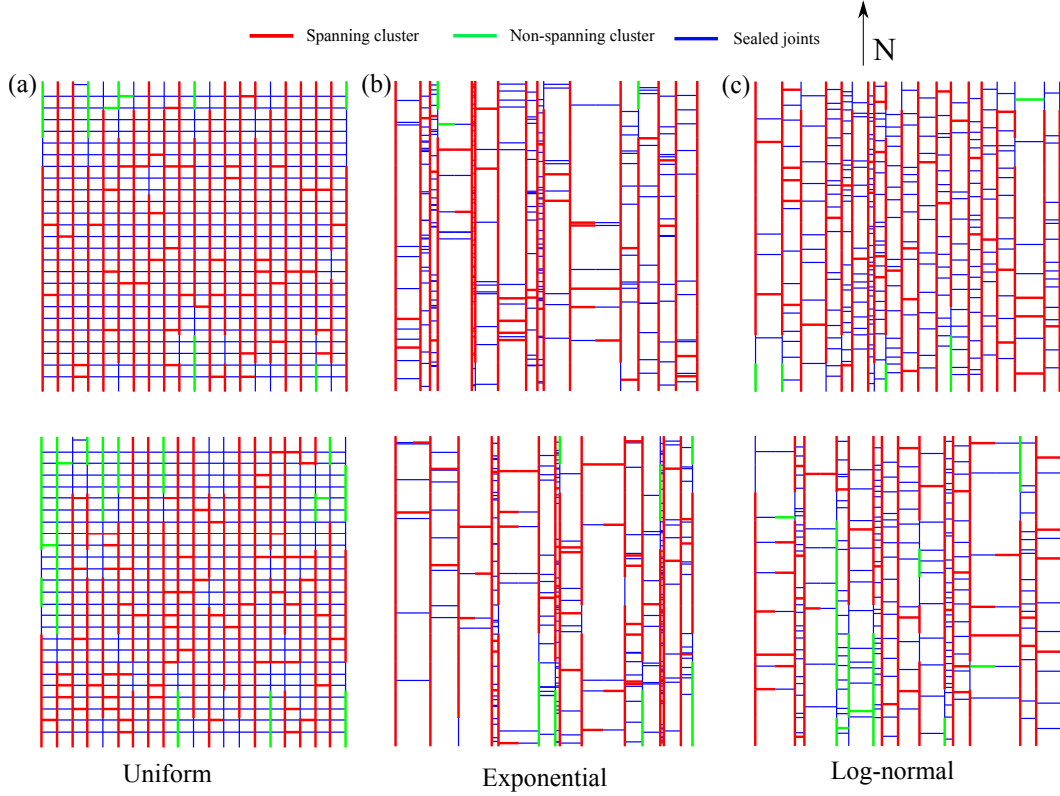


**Figure 6.** 2D orthogonal fracture networks with (upper panels) elliptical-shaped apertures; and (lower panels) log-normal distributed apertures. Preexisting joints have the NS strike, and cross joints have the EW strike; both preexisting and cross joints are spaced according to (a) uniform distribution; (b) exponential distribution; (c) log-normal distribution. The blue line segments indicate sealed fractures; the red line segments are open fractures and form a spanning cluster; the green line segments are open fractures that are locally connected.

$$P_{\text{span}} = \frac{N_{\text{span}}}{N_t}, \quad (5)$$

where  $N_t$  is the total number of realizations with a given fraction of open joints.  $N_t = 400$  and 100 for a 2D and 3D fracture network, respectively;  $N_{\text{span}}$  is the number of realizations with a spanning cluster formed in the system;  $P_{\text{span}}$  represents the frequency of forming a spanning cluster out of  $N_t$  realizations, and it is approximately equal to the probability of forming a spanning cluster under a given fraction of open joints. Because three parameters constrain all fracture networks, and each parameter has different values, the final results are stabilized by averaging over 150 random realizations of each fracture network. We developed an efficient in-house software, HATCHFRAC (Zhu et al., 2018, 2019), to perform the simulations. By extending the Newman–Ziff algorithm (Newman & Ziff, 2001), combined with a block method to check for clusters, the software efficiency is significantly improved. In Figs. 3 and 6, the red line segments refer to the spanning cluster formed in the system, while the green line segments are locally connected fractures.

## 2.4 Generation of a 3D orthogonal fracture network

Fractures not intersecting in the 2D space can still connect in the third dimension. To extend the sealing simulation and percolation analysis in 3D, we extend the 2D orthogonal fracture networks to three dimensions by assuming a  $90^\circ$  dip for each fracture (see Fig. 2). Non-vertical dip orientations are possible but more complex for implementation. A more complex scenario will not change the result significantly because the fracture network has been topologically well-connected with  $90^\circ$  dips. Furthermore, 3D fracture networks with  $90^\circ$  dips can keep all describing parameters the same as 2D fracture networks. Therefore, investigating differences caused only by dimensionality is possible. Each 3D fracture is represented by a rectangular plate, as shown in Fig. 7. To mimic the sealing of 3D fractures, each fracture is divided into small blocks. In the horizontal direction, each fracture is divided into small segments with a given segment length as in the 2D cases. In the vertical direction, each fracture is divided into four blocks. The aperture of each block is constant and follows one of the three distributions listed in Section. 2.2. The sealing mechanism is the same as in 2D orthogonal fracture networks, where it depends only on the block aperture. In the cluster-check process, only the fracture blocks with a line contact (block pair (1, 2) or (2, 3) in Fig. 7) are considered as intersecting each other. Fracture blocks with a point contact (block pair (1,3) or (4, 3) in Fig. 7) are not connected with each other.

The spanning cluster formed in the 3D fracture network connects the four peripheral faces of the system (excluding the upper and lower faces) to be consistent with the percolation criterion in 2D orthogonal fracture networks. Figs. 8 and 9 show the 3D orthogonal fracture networks with different aperture distributions.

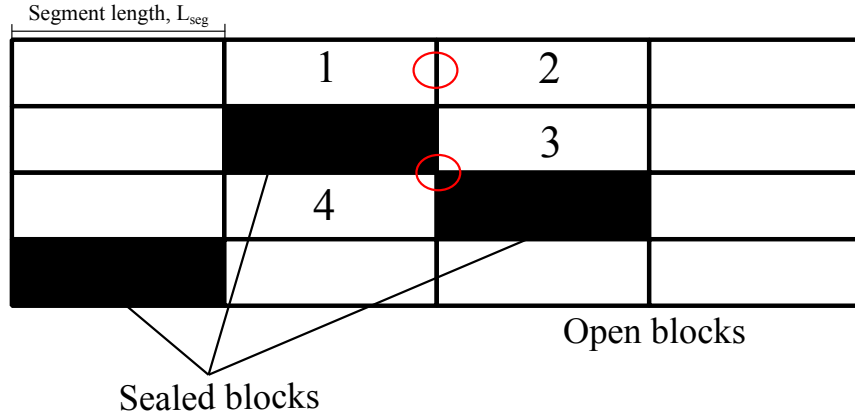


**Figure 7.** Segmentation of 3D fractures; each block has a constant aperture and can be sealed (black) or open (white). Only blocks with a line contact are connected (block pairs (1, 2) and (2, 3)); blocks with a point contact are disconnected (block pairs (1, 3) and (3, 4)). Blocks at different locations have different apertures.

In summary, we construct orthogonal fracture networks in two and three dimensions constrained by three parameters, apertures, segment lengths and spacing distributions of preexisting and cross joints. Different scenarios and values of each parameter are listed in Table. 1. Simulating the microscopic scale sealing, across millimeters, for example, is not practical because of the limited computational capacity. We select the decreasing segment lengths from 1 m to 0.2 m to show the trend of sealing at small scales. Because each parameter has three possible scenarios for each set of fractures, we have 81 possible combinations of the fracture networks composed of two sets of joints. For each fracture network with a chosen set of parameters, we seal a given fraction of fractures (ratio of lengths of sealed

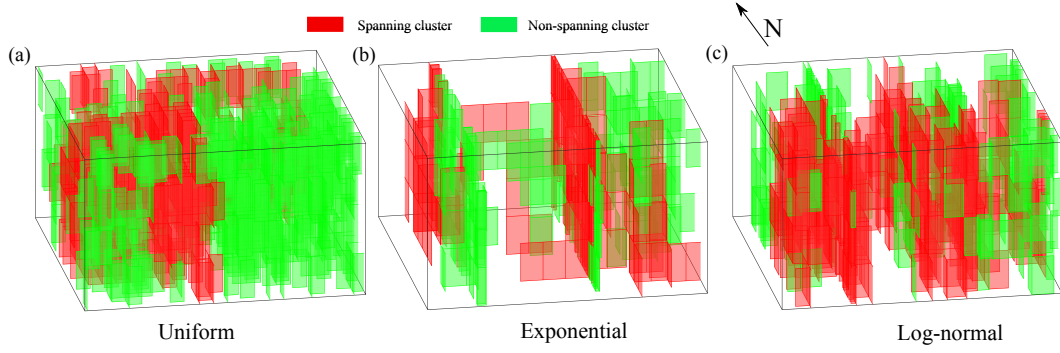


**Figure 8.** 3D orthogonal fracture networks with constant apertures. Preexisting joints have the NS strike, and cross joints have the EW strike. Both preexisting and cross joints are spaced according to (a) uniform distribution, (b) exponential distribution, and (c) log-normal distribution. Sealed fractures are not plotted for the clarity of the visualization. The red polygons are open fractures and form a spanning cluster, and the green polygons are open fractures that are locally connected. Vertical exaggeration = 16.

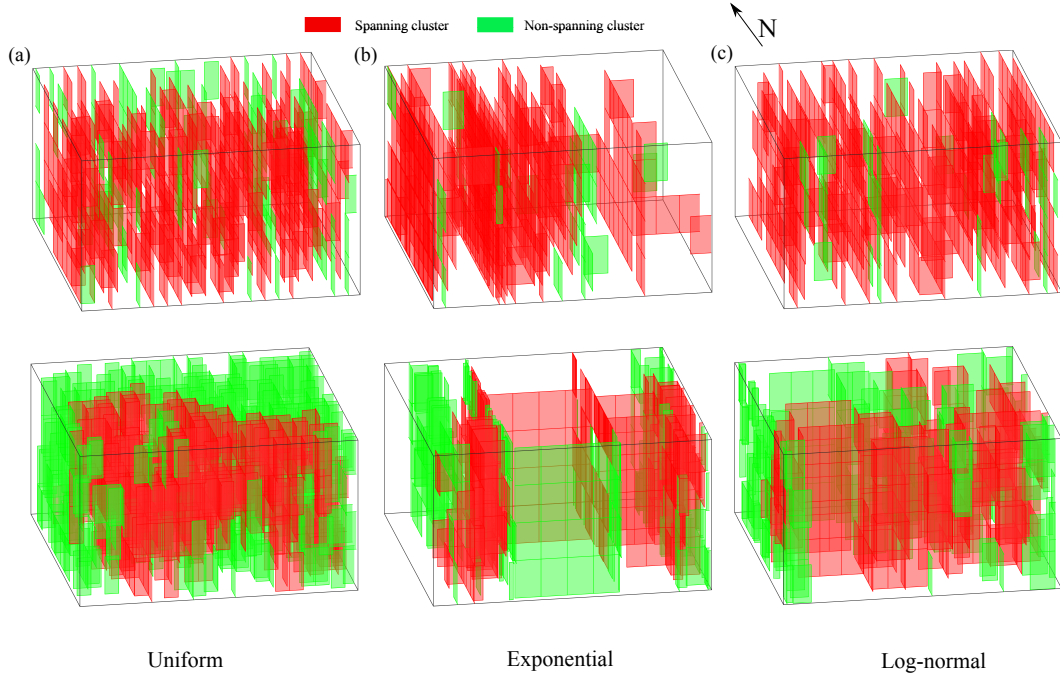


**Figure 9.** 3D orthogonal fracture networks with (upper panels) elliptical-shaped apertures; and (lower panels) log-normal distributed apertures. Preexisting joints have the NS strike, and cross joints have the EW strike. Both preexisting and cross joints are spaced according to (a) uniform distribution, (b) exponential distribution, and (c) log-normal distribution. Sealed fractures are not plotted for the clarity of the visualization. The red polygons are open fractures and form a spanning cluster, and the green polygons are open fractures that are locally connected. Vertical exaggeration = 16.

fractures to total fractures) and investigate the percolation state of the system. The final results are stabilized by averaging over 150 realizations per network.



**Table 1.** Scenarios for the constraining parameters

Parameter	Scenario 1	Scenario 2	Scenario 3
Aperture	Constant	Elliptical-shaped	Log-normal
Segment length, $L_{\text{seg}}$ , [m]	1	0.5	0.2
Spacing distribution	Uniform	Exponential	Log-normal

### 3 Results

Nine combinations of parameters per preexisting and cross joints network yield 81 combinations of parameters. However, these different combinations show similar trends and results. In this section, we offer the results for fracture networks, in which both preexisting and cross joints follow the same scenario for each parameter.

The percolation probability *vs.* the fraction of open joints of each orthogonal fracture network in 2D and 3D is shown in Fig. 10.

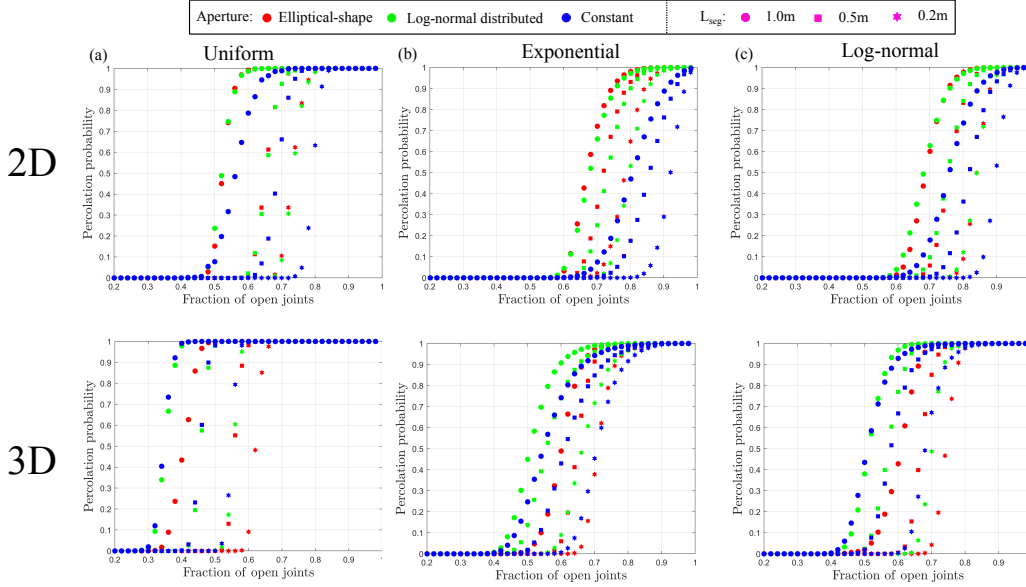


**Figure 10.** Percolation probability *vs.* fraction of open joints in 2D (upper panels) and 3D (lower panels) orthogonal fracture networks. Columns (a), (b), and (c) refer to orthogonal fracture networks with spacing distributions of preexisting and cross joints following the uniform, exponential and log-normal distributions, respectively.

Several observations for the 2D orthogonal fracture networks are summarized from the upper panels of Fig. 10

1. The percolation probability increases with the increasing fraction of open joints.
2. The red and green symbols are located to the left of the blue symbols. This pattern suggests that fracture networks with elliptical-shaped (red symbols) and log-normal distributed (green symbols) apertures form spanning clusters more easily than when the apertures are constant (blue symbols).

3. The data points in (b) and (c) are more to the right of the graph than in (a). This pattern means that the fracture networks with spacing that follows exponential (b) and log-normal (c) distributions have more difficulty in forming spanning clusters than do fracture networks with spacing following a uniform distribution (a).
4. As the segment length decreases, forming spanning clusters becomes increasingly difficult. In (c), more than 90 per cent of open joints are needed to form a spanning cluster. In reality, the sealed segment length can be a millimeter long. The fraction of sealing is usually severe; therefore, it is generally impossible to form a spanning cluster over a macroscopic fracture network.

In 3D orthogonal fracture networks, most observations in 2D remain valid. Compared with the 2D results, the data points are located more to the left in 3D, indicating that percolation in 3D fracture networks is more accessible. In contrast to the 2D cases, the red and green symbols are not always located on the left side of the blue symbols, suggesting that aperture variations do not always positively impact percolation in 3D fracture networks.

In Fig 11, we show the standard deviations of the percolation probability with error bars in different fracture networks. We choose the fracture networks with the log-normal distributed apertures and the uniform or log-normal spacing distributions to demonstrate the variations in the percolation probability. The remaining fracture networks behave similarly. For fracture networks with uniform spacing of the preexisting and cross joints, the standard deviations of the percolation probability are small, and variations are caused by the random sealing of fracture segments based on the aperture distribution. For fractures with log-normal spacing distributions, the standard deviations are significantly increased because variations are attributed to both the spacing distribution and aperture variations. The spacing distribution of preexisting and cross joints can substantially change the configuration of the fracture network. Compared with aperture variations, the spacing distribution makes more essential impacts on the percolation probability.

In brief, it is impossible to form a spanning cluster in a real subsurface fracture network because of the small segment lengths and severe sealing, which means that global connectivity is not practical. Without spanning clusters, local clusters can still contribute to the fluid flow in the subsurface if their size is large enough. Figs. 12 and 13 show the relative size of the largest fracture cluster for each case averaged with over 150 realizations in 2D and 3D fracture networks. When the spanning cluster forms, the largest cluster is the spanning cluster itself. Otherwise, the largest cluster is the largest locally connected cluster. The mean size of the cluster is not representative of local clusters, because many isolated fracture segments can significantly reduce the mean cluster mass.

As the percolation probability increases, the relative size of the largest cluster also increases. When the percolation probability reaches one and remains constant afterwards, the relative size also reaches a plateau. The relative size should continue to increase since more joints are open. However, since the cluster-check algorithm is time-consuming, we stop checking clusters with more fracture segments when a spanning cluster forms, and this causes the relative size to remain unchanged. Forming a spanning cluster, in reality, is almost impossible. Therefore, this simplification is insignificant to the overall analysis. The left parts of Figs. 12 and 13, where the fraction of open joints is smaller than 0.5, are more important because real fracture networks may experience severe sealing. When the fraction of sealing is large, i.e., more than 50%, the relative size of the largest cluster is small and decreases with the segment lengths. Fig. 14 (a) shows the percolation probability and relative size of the largest cluster in a fracture network with segment lengths of 0.05 m. The aperture and spacing of the fracture network follow a log-normal distribution. If 10% of the fractures are sealed, the probability of forming a spanning cluster is 0. If 50% of fractures are sealed, the relative size of the largest cluster is smaller than 0.1%. Fig. 14 (b) shows one realization of such a fracture network with 50% of fractures sealed. No spanning cluster is formed, and the largest cluster (red line segments) is small in size.

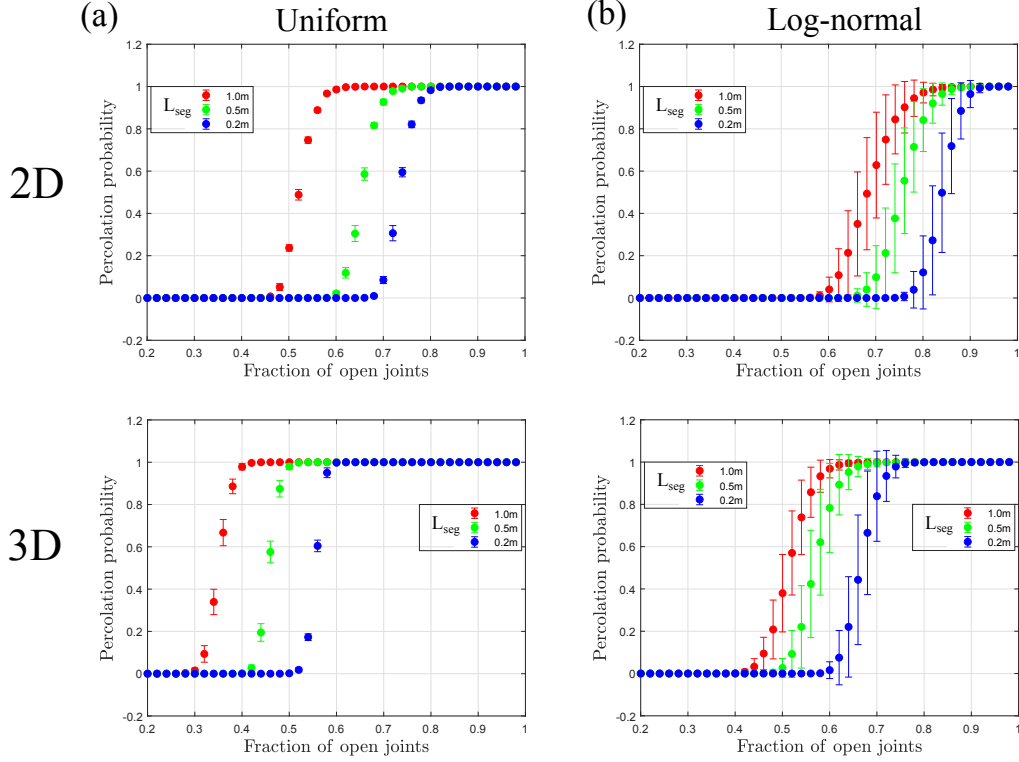


**Figure 11.** Percolation probability *vs.* fraction of the open joints with error bars in the 2D (upper panels) and 3D (lower panels) orthogonal fracture networks. Fracture networks have apertures following a log-normal distribution. Columns (a) and (b) refer to orthogonal fracture networks with spacing distributions of preexisting and cross joints following the uniform and log-normal distributions, respectively.

## 4 Discussion

Based on our observations and analysis in the previous section, we draw two main conclusions: first, real subsurface fractures are most likely to be partially sealed, and they cannot form a spanning cluster; second, real subsurface fractures can form locally connected open clusters, and these clusters are small in size. These conclusions can provide answers to the questions posed in the Introduction.

### 4.1 Q1 and Q2: Why do non-critically stressed fractures usually show non-hydraulic responses, and what are the possible reasons for the occurrence of any exceptions?

Under the current stress state, critically stressed fractures contribute to fluid flow regardless of whether they were entirely sealed or open before sliding, and they show good hydraulic responses. Fractures with non-critical orientations are mechanically stable and do not slip. One possible reason why they show non-hydraulic responses is that they are partially or completely sealed. If the orthogonal fracture network (with non-vertical dips) shown in Fig. 14 (b) exists in the subsurface formation, and if a well intersects this fracture network, the well is most likely to encounter sealed fractures or small, locally connected clusters of open fractures. None of these fractures provides a large enough flow to exhibit significant hydraulic responses. However, if the well encounters a local cluster that is large enough, it is still possible to have a limited hydraulic response. This possibility explains

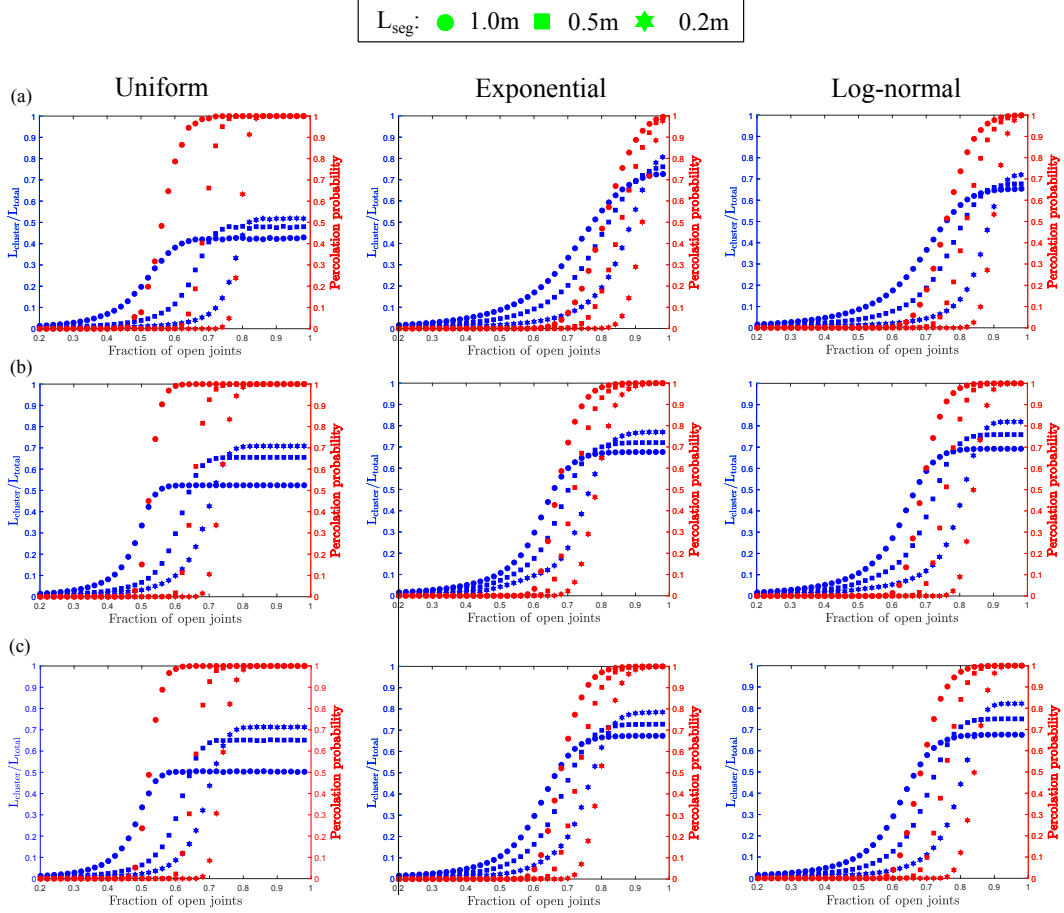


**Figure 12.** The relative size of the largest cluster in 2D orthogonal fracture networks. Left  $y$ -axis: relative size of the largest cluster (blue symbols); right  $y$ -axis: percolation probability (red symbols). Left to right columns: orthogonal fracture networks with spacing distributions of preexisting and cross joints following the uniform, exponential and log-normal distributions, respectively; upper row (a) to lower row (c): orthogonal fracture networks with apertures following the constant, elliptical-shaped and log-normal distributions, respectively.

the exceptions occurring in Fig. 1, where a few hydraulically conductive fractures have their stress mapping points far away from the failure line in the Mohr diagram.

#### 4.2 Q3: Importance of non-critically stressed and partially sealed fractures

This section demonstrates the importance of critically-stressed fractures and emphasizes the importance of non-critically stressed and partially sealed fractures. In a hydraulic fracturing process, the former fractures generate the stimulated reservoir volume (SRV), while the latter enlarge the SRV and contribute to production.

We assume a stable strike-slip stress state ( $Sh_{\min} < S_v < Sh_{\max}$ ) in a given subsurface formation. Set  $S_v = 1$  as the reference stress with  $Sh_{\max} = 1.3S_v$ ,  $Sh_{\min} = 0.8S_v$  and  $P_p = 0.5S_v$ , where  $Sh_{\max}$ ,  $Sh_{\min}$ ,  $S_v$  and  $P_p$  are the maximum horizontal stress, minimum horizontal stress, vertical stress and reservoir pressure. Fig. 15 shows the map view of the formation, and the stress state of any location (the blue element, for example) in the formation is shown in the Mohr diagram (blue circle). All fractures in this formation are in a

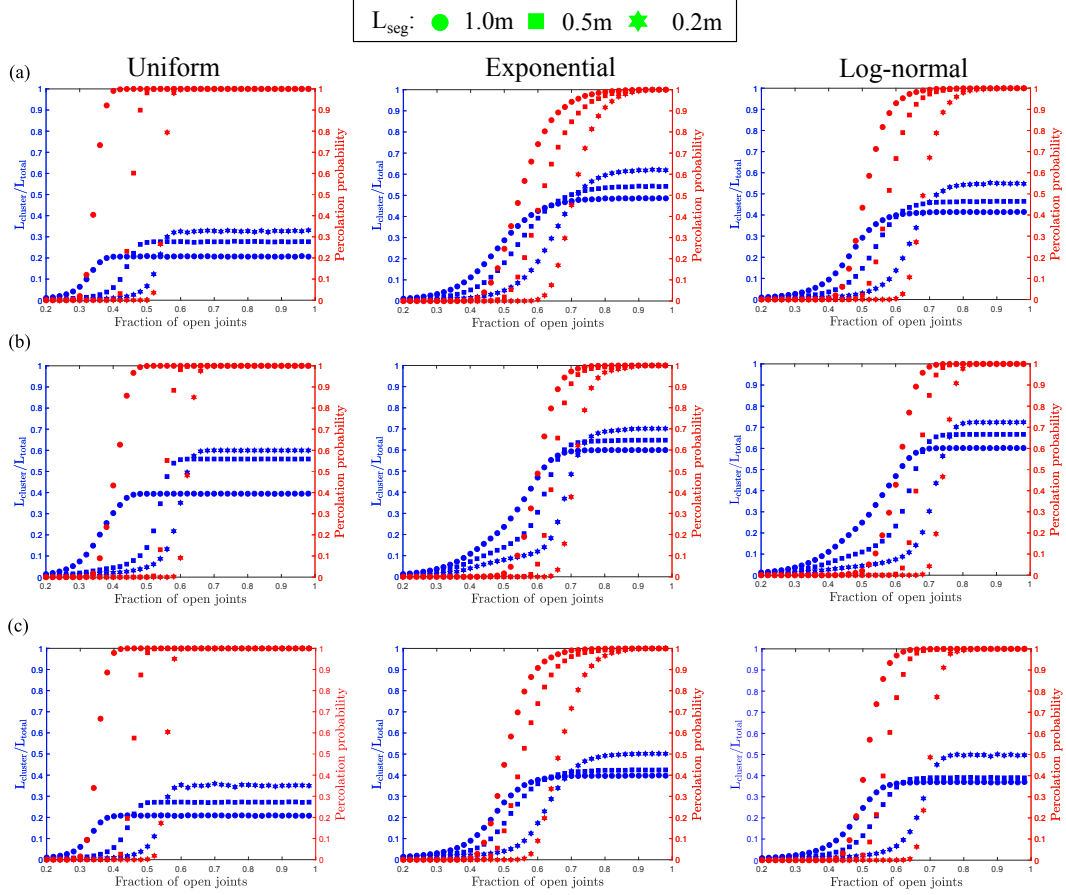


**Figure 13.** The relative size of the largest cluster in 3D orthogonal fracture networks. Left  $y$ -axis: relative size of the largest cluster (blue symbols); right  $y$ -axis: percolation probability (red symbols). Left to right columns: orthogonal fracture networks with spacing distributions of preexisting and cross joints following the uniform, exponential and log-normal distributions, respectively; upper row (a) to lower row (c): orthogonal fracture networks with apertures following the constant, elliptical-shaped and log-normal distributions, respectively.

non-critically stressed state, and they are partially or completely sealed over geological time. However, if there is a significant stress perturbation, such as hydraulic fracturing, the stress state close to the hydraulic fracture will change. Hydraulic fracturing is essential for the exploitation of unconventional reservoirs, such as shale gas reservoirs, because it generates the SRV or the complex fracture network that surrounds the hydrofracture and contributes to production (Mayerhofer et al., 2010).

In formations with low permeability, natural fractures play an important role in forming SRV. Here, we consider a conceptual model with only one hydraulic stage with one perforation cluster to demonstrate the importance of natural fractures. The hydraulic fracture that originates from the perforation is denoted as the primary hydraulic fracture. We assume that the fluid pressure is uniform along the primary hydraulic fracture. From the simulation and analysis of Warpinski et al. (2013, 2001), the principal stresses near the hydraulic fracture increase because of the high fluid pressure in the hydraulic fracture. The increase in the principal stresses declines sharply with increasing distance from the hydraulic fracture. The red Mohr's circle in Fig. 15 shows the stress state of the blue element after hydraulic fracturing. The Mohr's circle shrinks and moves rightward, which means that the increase

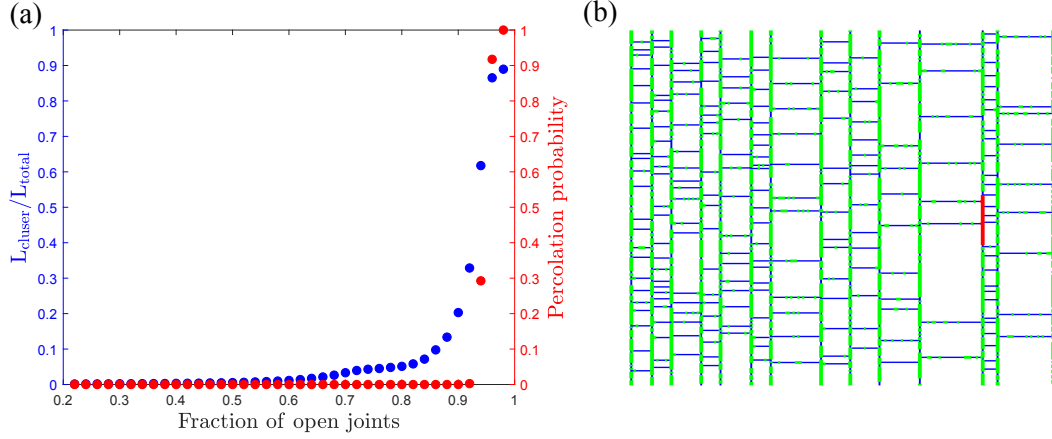


**Figure 14.** (a) The relative size of the largest cluster and the percolation probability in the orthogonal fracture network. (b) A 2D orthogonal fracture network with a segment length of 0.05 m and 50% of joints sealed. The blue line segments are sealed joints; the red line segments are the largest cluster; the green line segments are the remaining local clusters. Apertures follow a log-normal distribution, and the spacing follows a log-normal distribution for both preexisting and cross joints.

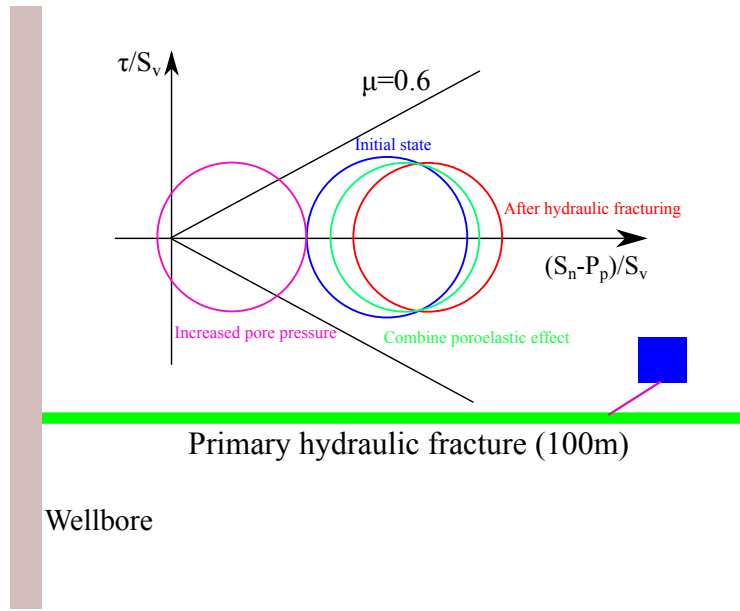


**Figure 15.** Map view of a subsurface formation. The Mohr diagram shows the stress state of the blue element at the initial state (blue), after considering the changes of principal stresses caused by the hydraulic fracturing (red), after considering the poroelastic effect (green), and after considering the high fluid pressure transmitted through natural fractures (purple).

in the principal stresses stifles any possible microseismicity from occurring in this region. Due to the poroelastic effect, the increase of stresses can also cause an increase in pore pressure. If we assume that the system is water-saturated and in an undrained condition, the increase in pore pressure can be estimated as the mean increase of the three principal stresses (Biot, 1941):

$$\Delta P_p = \frac{1}{3}(\Delta\sigma_1 + \Delta\sigma_2 + \Delta\sigma_3). \quad (6)$$

The green Mohr's circle shows the stress state after considering the poroelastic effect. The poroelastic effect is not essential for low-permeable formations (Warpinski et al., 2001), and it cannot cause natural fractures to slide because the Mohr's circle is still far away from the failure line. One possibility is that the fluid pressure in the primary hydraulic fracture can be transmitted to the neighbouring region through natural fractures (purple fracture between the blue element and the primary hydraulic fracture). The corresponding Mohr's circle is shown in purple in Fig. 15. Natural fractures with a wide range of orientations can slide or even experience tensile failure under this stress state.

With the elevated pore pressure, natural fractures in critical orientations can reach the critically stressed state and form SRV. To visualize the SRV composed of critically stressed fractures is almost impossible, because we do not know the actual configurations of the fracture networks in the subsurface. With the DFN modelling software, we further construct a conceptual reservoir model with background fractures to demonstrate the importance of both critically and non-critically stressed fractures.

We assume that the shale formation has a background fracture network with a system size of 50 m, shown in Fig. 16. Fracture orientations follow a uniform distribution between 0 and  $\pi$ , because the fractures may have random orientations from complex stress changes over a long geological period. Fracture center positions follow a uniform distribution. Apertures are constant, and 50% of the fractures are sealed with a segment length of 1 m. The fracture lengths follow a power-law distribution with an exponent of 3.0, which makes most fractures short (1 to 3 m). From the observations of microseismicity induced by hydraulic fracturing, most microearthquakes have a degree of -2 (Maghsoudi et al., 2016), which corresponds to a fault patch size of 1 to 2 meters (Zoback & Gorelick, 2012). The fracture network is well connected by adding more fractures after the formation of the spanning cluster. If  $N_p$  is the number of fractures required to form the spanning cluster in the system, we generate  $1.0 \sim 2.5 N_p$  fractures to ensure good connectivity of the fracture network. Several assumptions are required to visualize the stimulated reservoir volume.

- The elevated pore pressure of the primary hydraulic fracture equals the reference stress,  $S_v$ .
- The pore pressure at the upper and lower boundary of the system is the reservoir pressure ( $0.5 S_v$ ).
- The pore pressure dissipates from the primary hydraulic fracture linearly with the distance to the hydraulic fracture.
- Coulomb failure criterion with  $\mu = 0.6$  is used to distinguish critically and non-critically stressed fractures.

In Fig. 16, the red cluster is composed of the primary hydraulic fracture and open fractures that intersect the primary hydraulic fracture. This cluster yields a small conductive fracture length and contributes slightly to shale gas production. Therefore, the SRV generated during hydraulic fracturing is the main contributor to shale gas production rather than the hydraulic fracture itself.

Fig. 17 shows the critically stressed fractures located away from the primary hydraulic fracture. Purple and red fractures are in critical orientations, while red fractures are connected to the primary hydraulic fracture either directly or indirectly. Only red fractures are critically stressed because they have connected pathways for the transmission of high-pressure fluid. Since the fluid pressure dissipates as it travels through natural fractures, the effective stresses increase when the fractures are far away from the primary hydraulic fracture. In Fig. 17, we show possible stress states at four different locations. The corre-



sponding range of critical orientations shrinks (the red arcs in Fig. 17), and the fracture intensity decreases accordingly. When the Mohr's circle is tangent to the failure line, no natural fractures can slide. Note that not all critically stressed fractures can trigger a microearthquake. Most of them slide slowly and stably and are thus undetectable (Das & Zoback, 2013).

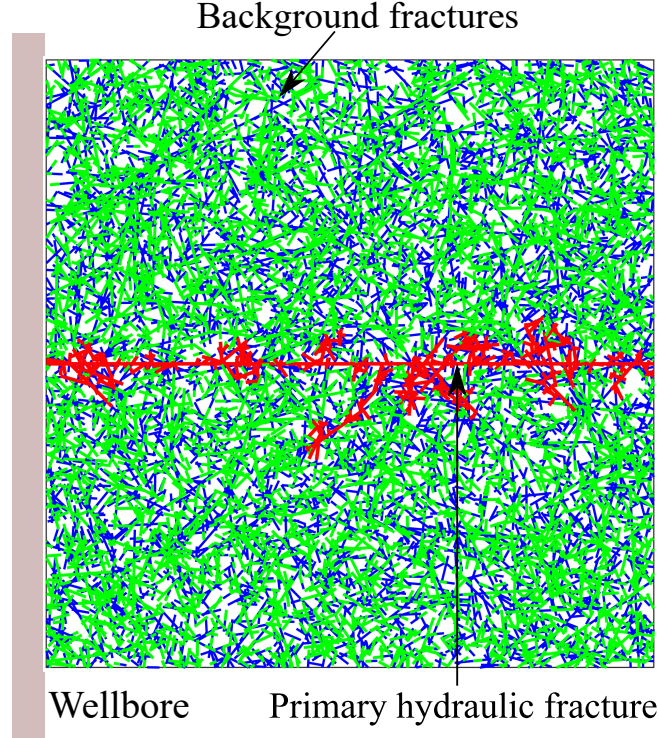


**Figure 16.** Map view of a subsurface formation with background fractures (blue: sealed; green: open). The red line segment is the primary hydraulic fracture; 50% of the background fractures is sealed.

In Fig. 17, only fractures with critical orientations are presented. However, non-critically stressed fractures can also contribute to fluid flow, because they are partially sealed and form locally connected open clusters. Fig. 18 shows a connected open fracture network after including the non-critically stressed and partially sealed fractures. The size of the open fracture cluster connected to the primary hydraulic fracture is significantly enlarged. In linear flow, the flux from the matrix to the fractures is proportional to the fracture area (Bello et al., 2010; Syed Haider & W., 2020), suggesting that partially sealed fractures can increase reservoir production by enlarging the stimulated reservoir volume. We test fracture networks with different amounts of additional fractures, and list the contribution of non-critically stressed and partially sealed fractures in Table 2. Renshaw et al. (2020) argued that only limited fracture growth is possible after the onset of percolation. However, this should be true for fractures of the same generation. For complex fracture networks composed of many sets of fractures after a long geological history, their intensities can be significantly larger than the intensity at percolation, which is observed in many outcrop maps (C. C. Barton, 1995; Watkins et al., 2015). One example of outcrop maps at Achnashellach Culmination field area (Watkins et al., 2015) is shown in Fig. 19, where the largest cluster is marked in red, and the other small clusters are marked in green. The outcrop is processed with an automatic fracture detection algorithm (Zhu et al., 2020), where raw outcrops are converted to polylines for calculations. The increase of fracture

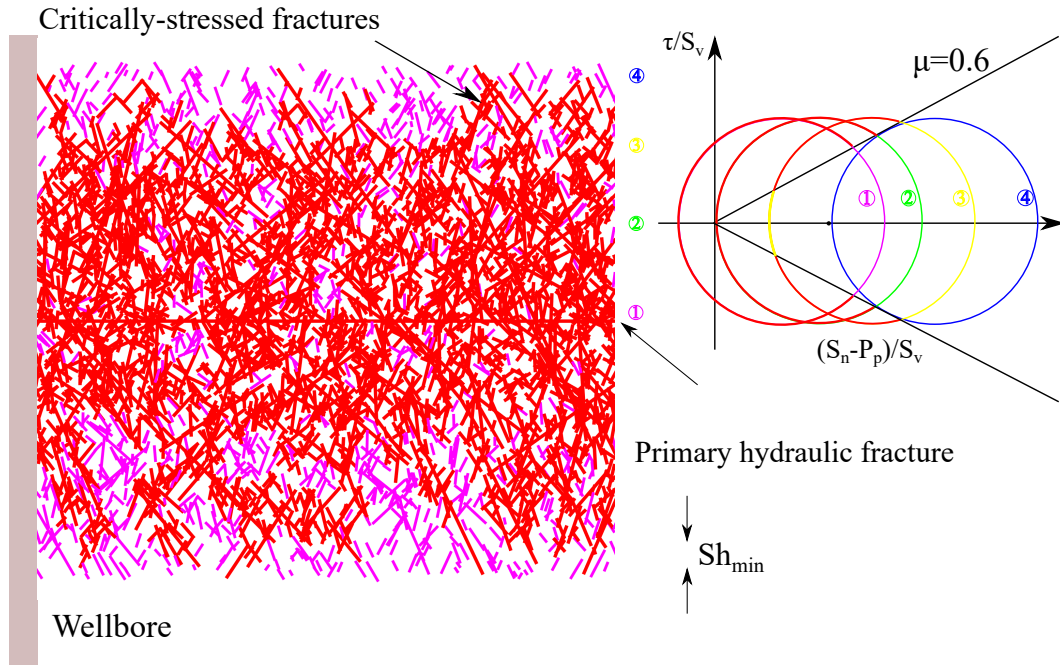


**Figure 17.** Map view of a subsurface formation. The purple and red fractures are in critical orientations; the red fractures are connected to the primary hydraulic fracture either directly or indirectly. The Mohr diagram shows the stress states of elements at different locations. The red arcs indicate the possible ranges of orientations to cause failure (either tensile or shear failure)

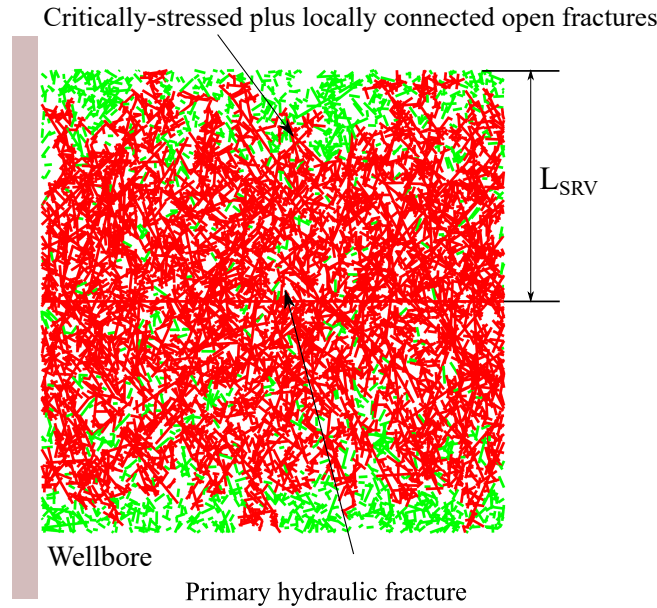


**Figure 18.** Map view of a subsurface formation. The green and red fractures are in critical orientations or locally open; the red fractures are connected to the primary hydraulic fracture either directly or indirectly.

length by non-critically stressed, and partially sealed fractures can be significant. The more fractures in the system, the better their connectivity is. The corresponding increase in frac-

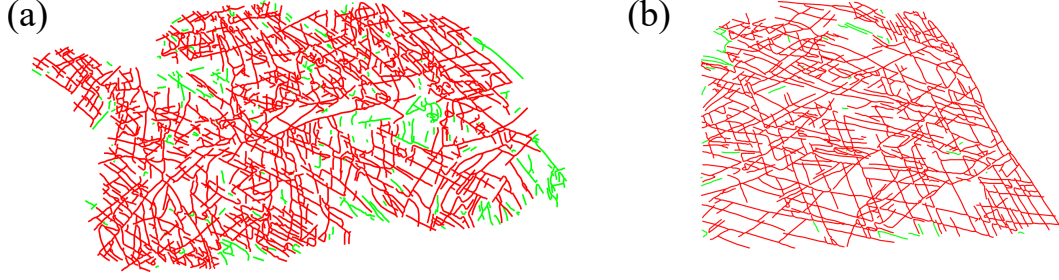


**Figure 19.** Fracture outcrop map at Achnashellach Culmination field area (Fig. 7B and 7D in Watkins et al. (2015)). Red line segments are the largest spanning cluster; Green line segments are local clusters.

ture length is also more significant. This is an approximate conclusion, and the impact of fracture intensities, fracture lengths and clustering effects on the enlargement of the SRV is investigated in our recent conference paper (Zhu, He, & Patzek, 2021).

**Table 2.** Contribution of non-critically stressed and partially sealed fractures

$N_f^a$	$L_c, [m]^b$	$L_b, [m]^c$	Increase, %
$1.00 \times N_p$	1,952	2,236	15
$1.25 \times N_p$	3,825	4,624	21
$1.50 \times N_p$	7,211	9,141	27
$1.75 \times N_p$	7,576	9,840	30
$2.00 \times N_p$	10,396	14,001	35
$2.50 \times N_p$	177,66	25,561	44

<sup>a</sup> the number of fractures in the system and  $N_p$  is the number of fractures needed to form a spanning cluster.

<sup>b</sup> the total length of all connected critically stressed fractures

<sup>c</sup> the total length of fractures including both connected critically stressed fractures and non-critically stressed and partially sealed fractures

#### 4.3 Estimation of the stimulated reservoir volume in 2D

In this section, we can further relax the assumption that the pore pressure at the upper and lower boundary of the system is the reservoir pressure, and estimate the physical distance that injected fluid can travel through natural fractures, which is also the size of SRV.

The stimulated reservoir volume (SRV) is usually estimated by the 3D volume of a microseismicity cloud (Mayerhofer et al., 2010). However, it is impossible to obtain the detailed structure of the SRV with existing fracture mapping tools. Warpinski et al. (2009); M. K. Fisher et al. (2002); M. Fisher et al. (2004, 2004) and Mayerhofer et al. (2006) assumed that an orthogonal fracture network spans SRV and investigated the importance of SRV on reservoir production. From the analysis of the aforementioned Mohr diagrams, it is obvious that natural fractures perpendicular to the primary hydraulic fracture are unlikely to slide and are always in a mechanically stable state. Therefore, the commonly adopted orthogonal configuration of SRV is unrealistic in general.

In this section, we investigate SRV structure in more detail and estimate the SRV in a simple but physically meaningful way. In a 2D map view, SRV is determined by  $L_{SRV}$  in Fig. 18, which maps the farthest distance for the occurrence of fracture slippage. To estimate  $L_{SRV}$ , we separate this distance into two parts: the limiting distance for generating hydraulic fractures,  $\Delta L_h$ , and the limiting distance for making natural fractures slide,  $\Delta L_s$ .

Raterman et al. (2018) and Marder et al. (2015) showed that multiple hydraulic fractures besides the primary hydraulic fracture can be generated during the hydraulic fracturing process. The generated hydraulic fractures can originate from cracks near the horizontal wellbore and along the primary hydraulic fractures or other forms of weak planes. They can take most of the injected fluid. Fig. 20 shows the generation of multiple hydraulic fractures.

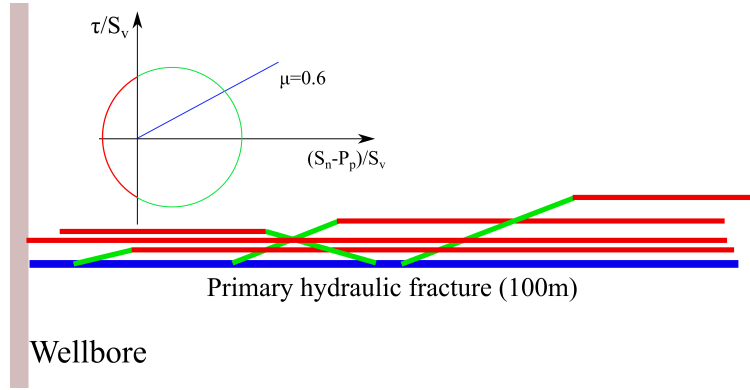


**Figure 20.** Map view of a subsurface formation to demonstrate the generation of hydraulic fractures from natural fractures. The red line segments indicate the hydraulic fractures originating from the cracks near the wellbore and along the primary hydraulic fracture. The green line segments are natural fractures in critical orientations. The Mohr diagram shows a typical stress state of a green fracture plane. The red arc in the Mohr's circle indicates the potential orientations for green fractures to form a hydraulic fracture.

To generate a hydraulic fracture, the pore pressure has to be larger than  $Sh_{min}$ . However, the fluid pressure dissipates when the fluid flows farther away from the primary hydraulic fracture (Marder et al., 2015). Beyond a certain distance, the pore pressure will be insufficient to break rock and form hydraulic fractures (blue line in Fig. 21), but it is still large enough to cause slipping of natural fractures and to generate more complex fracture networks. To estimate the limiting distance to create hydraulic fractures, we consider the simple architecture of a natural fracture network shown in Fig. 21.

Several assumptions are required:

- The primary hydraulic fracture has a half-length of 100 m and a height of 100 m;
- The fluid pressure along the primary hydraulic fracture is uniform and 500 psi (3.44 MPa) higher than the  $Sh_{min}$ ;
- Natural fractures are square plates with the length and height of 1 m. Once the pore pressure is large enough to open a natural fracture, its height jumps to 100 m, and the fracture propagates in the direction of  $Sh_{max}$ .
- The injection rate is  $0.1 \text{ m}^3/\text{s}$  in each direction and remains constant. Eighty per cent of fluid goes to the hydraulic fractures initiating from natural fractures. The total

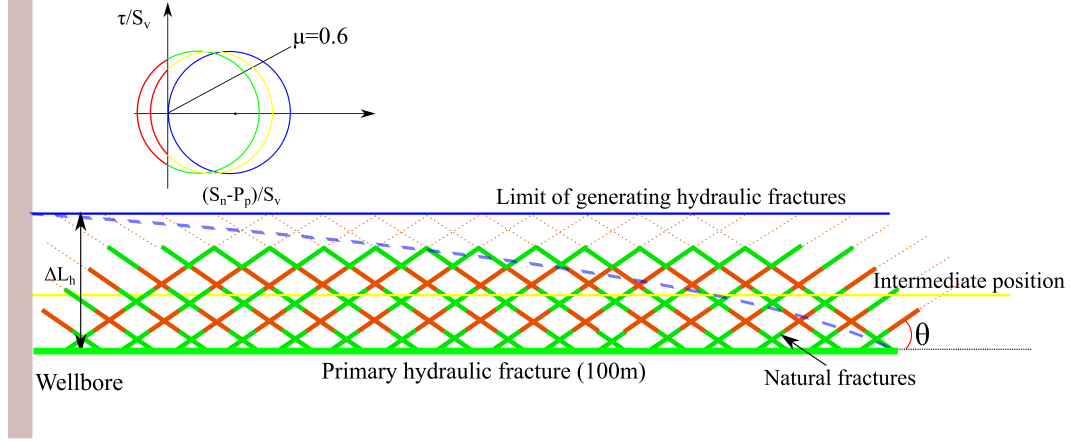


**Figure 21.** Map view to demonstrate the limit of generating hydraulic fractures. The natural fractures form a conjugate fracture network and are marked in green and red, respectively, to show that each fracture is 1 m long. The Mohr diagram shows the stress state of fracture network elements at different locations (green: the primary hydraulic fracture; yellow: the intermediate locations; blue: the limit of generating hydraulic fractures). The red arcs in Mohr's circles indicate the possible orientations of natural fractures to generate mode-1 hydraulic fractures since the effective normal stress is tensile. The possible orientations are close to that of the primary hydraulic fracture. The blue dashed line is the modified limit of generating hydraulic fractures, with the pore pressure in the primary hydraulic fracture declining towards the toe.

- 539 flow rate in those natural fractures on one side of the primary hydraulic fracture is  
 540 thus  $0.04 \text{ m}^3/\text{s}$ .
- 541 • The natural fractures form a conjugate system, also shown in Fig. 21, because natural  
 542 fractures are assumed to have uniform orientations from  $0$  to  $\pi$ , and the stress tensor  
 543 is symmetrical.
  - 544 • The average strike angle,  $\theta$ , is  $15^\circ$ . In Fig. 21, the red arcs indicate stress mapping  
 545 points of possible fractures to initiate new hydraulic fractures. They have orientations  
 546 close to the primary hydraulic fracture and decrease with increasing distance.
  - 547 • The pore pressure at the blue line in Fig. 21 is equal to  $S_{h_{\min}}$ . Therefore, beyond the  
 548 blue line, no more hydraulic fractures can be generated.
  - 549 • The apertures of the hydraulically open fractures are proportional to the net pressure.  
 550 The average aperture is assumed to be  $2 \times 10^{-4} \text{ m}$ , and the permeability of fracture,  
 551  $k$ , follows the cubic law.
  - 552 • Darcy's law is applicable to fluid flow in the fractures.
  - 553 • The viscosity,  $\mu$ , of injected fluid is one cP.

554 Since the flow from any inlet at the primary hydraulic fracture to the corresponding outlet  
 555 at the limiting distance has the same boundary condition, we can apply Darcy's law along  
 556 any flow path in Fig. 21:

$$Q_f = -\frac{kA}{\mu} \frac{\Delta p}{\Delta L_h / \sin(\theta)} \quad (7)$$

$$Q_f = \frac{0.1 \times 0.8 \times 0.5}{N/(\Delta L_h/\sin(\theta))}, \quad (8)$$

where  $A$  is the cross-sectional area [ $\text{m}^2$ ];  $N$  is the number of fractures in the half domain (one side of the primary hydraulic fracture) shown in Fig 21;  $\frac{N}{\Delta L_h/\sin(\theta)}$  is the number of inlets that can be regarded as the number of hydraulic fractures if each inlet fracture can form a hydraulic fracture. From Raterman et al. (2018)'s observations, there can be more than 100 hydraulic fractures formed in one stage. Combining Eqs. (7) and (8), we have

$$\Delta L_h = -\frac{kA}{\mu} \frac{\Delta p \times \sin(\theta)}{Q_f} \quad (9)$$

- If  $N = 500$ ,  $\Delta L_h = 13.9$  m and number of inlets is 9.
- If  $N = 1000$ ,  $\Delta L_h = 19.6$  m and number of inlets is 13.
- If  $N = 5000$ ,  $\Delta L_h = 43.8$  m and number of inlets is 30.

The limiting distance along the generating hydraulic fractures ranges from ten to several tens of meters, and its value depends on the natural fracture intensity and their geometry (sizes and apertures). In reality, the pressure distribution is not uniform along the primary hydraulic fracture, but decreases toward the toe (Warpinski et al., 2001; Marder et al., 2015), suggesting that the limit of generating hydraulic fractures, the blue line in Fig. 21, should not be horizontal but inclined toward the toe (dashed line in Fig. 21). The intensity of hydraulic fractures should also be higher in the region close to the heel because of the high fluid pressure there, which is consistent with the observation of Raterman et al. (2018).

When a fluid travels beyond the limiting distance along the generating hydraulic fractures, the fluid pressure is still sufficient to cause natural fractures to slide and create a more complex fracture network. Apertures associated with sliding are enlarged by shear displacement, but they are considerably smaller than the apertures induced by tensile failures. At the limiting distance where no more natural fractures can slide, the Mohr's circle is tangent to the failure line. Fig. 22 includes a sketch map of fracture networks formed by the sliding natural fractures. A few different assumptions are made for this case:

- The difference between  $\text{Sh}_{\min}$  and reservoir pressure is 10 MPa.
- Natural fractures are rectangular plates with the length and height of 1 m. Natural fractures do not propagate after sliding.
- The  $\theta$  value is larger in the sliding cases as we observe from the Mohr diagram in Fig. 22. The average  $\theta$  value is set at 40 degrees.
- Ten per cent of injected water flows into the sliding fracture network. Since natural fractures do not propagate after sliding, the fluid is stored in the volume of natural fractures. If we assume that  $400 \text{ m}^3$  of water is injected in one stage per half-hydraulic fracture, the corresponding number of natural fractures in the half domain is  $N = 400 \times 10\%/2/(a \times 1 \times 1)$ .

With the same formula as Eq. (9), we have

- If  $a = 3.5 \times 10^{-6}$  m,  $\Delta L_s = 4.1$  m, and  $N = 5.7 \times 10^6$
- If  $a = 1.0 \times 10^{-5}$  m,  $\Delta L_s = 11.7$  m, and  $N = 2.0 \times 10^6$
- If  $a = 2.0 \times 10^{-5}$  m,  $\Delta L_s = 23.5$  m, and  $N = 1.0 \times 10^6$

The limiting distance of making natural fractures slide ranges from ten to several tens of meters, and its value is sensitive to the permeability of the natural fractures. Since the limit of generating hydraulic fractures is inclined towards the toe, the limit of sliding natural fracture should also be inclined (the dashed line in Fig. 22).



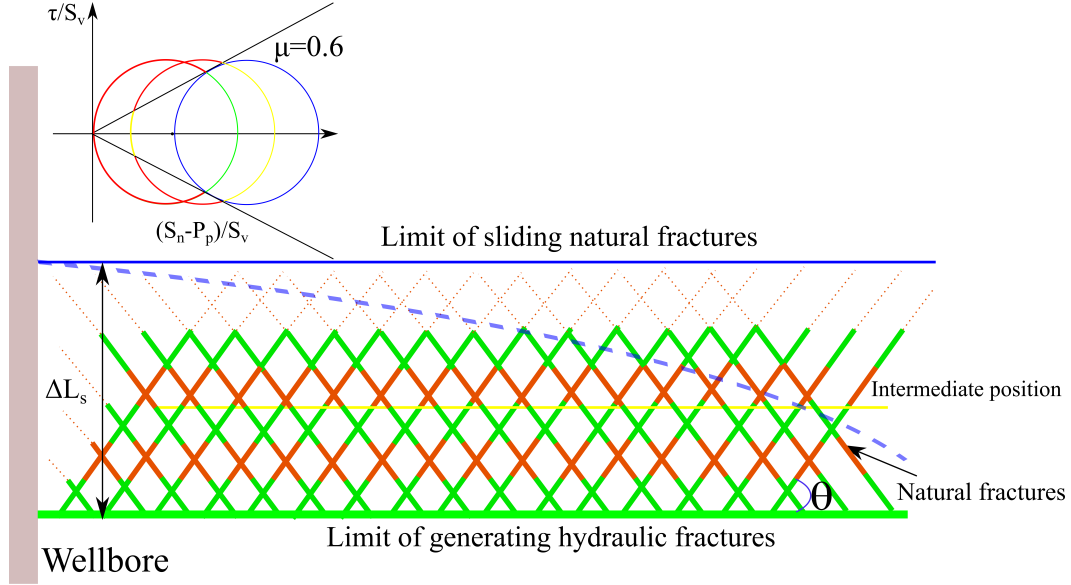


**Figure 22.** Map view to demonstrate the limit of sliding natural fractures. The natural fractures form a conjugate fracture network and are marked in green and red, respectively, to show that each fracture is 1 m long. The Mohr diagram shows the stress state of network elements at different locations (green: the limit of generating hydraulic fractures; yellow: the intermediate positions; blue: the limit of sliding natural fractures). The red arcs in Mohr's circles indicate the possible orientations of natural fractures that cause sliding. The blue dashed line is the modified limit of sliding natural fractures, because the limiting distance for generating hydraulic fractures decreases towards the toe.

Combining  $\Delta L_h$  and  $\Delta L_s$  leads to  $L_{SRV}$ , and its value varies between 20 to 70 m depending on the intensity of natural fractures and the permeability they have after the stimulation. The elongated shape of SRV is consistent with patterns found in microseismic cloud maps (Rateman et al., 2018; Shaffner et al., 2011).

## 5 Conclusions

In this paper, we simulate the sealing of 2D and 3D orthogonal fracture networks, and investigate the impact of such sealing on the percolation state of the fracture network. Furthermore, we perform simulations to answer fundamental questions related to hydrofracturing. Several key conclusions emerge:

- A small amount of sealing can prevent the formation of spanning clusters in 2D and 3D fracture networks.
- Fractures are most likely to be partially sealed, and they can form locally connected open clusters, which are small in size.
- Without significant stress perturbations, most fractures are partially sealed and non-critically stressed, and they usually do not contribute much to fluid flow. However, under a significant stress perturbation, such as hydrofracturing, the well-connected and critically oriented fractures become critically stressed and slide because of the elevated pore pressure, whereas the partially sealed and non-critically stressed fractures can also contribute to the flow by enlarging the stimulated reservoir volume.



- Estimation of the stimulated reservoir volume can be split into two parts. One is the limiting distance along the generating hydraulic fractures,  $\Delta L_h$ , and the other is the limiting distance of making natural fractures slide,  $\Delta L_s$ . A rough estimation yields an elongated shape of the SRV, which is consistent with observations from microseismic cloud maps.

## Acknowledgement

This project was supported by baseline research funding from KAUST to Prof. Tad W. Patzek. All the synthetically generated data are available online:  
<https://doi.org/10.4121/14602119.v1>

## References

- Bai, T., Maerten, L., Gross, M. R., & Aydin, A. (2002). Orthogonal cross joints: do they imply a regional stress rotation? *Journal of structural geology*, 24(1), 77–88.
- Bai, T., Pollard, D., & Gao, H. (2000). Explanation for fracture spacing in layered materials. *Nature*, 403(6771), 753–756.
- Bai, T., Pollard, D. D., & Gross, M. R. (2000). Mechanical prediction of fracture aperture in layered rocks. *Journal of Geophysical Research: Solid Earth*, 105(B1), 707–721.
- Barton, C. A., Zoback, M. D., & Moos, D. (1995). Fluid flow along potentially active faults in crystalline rock. *Geology*, 23(8), 683–686.
- Barton, C. C. (1995). *Fractals in the earth sciences*. Springer.
- Becker, S., Eichhubl, P., Laubach, S., Reed, R., Lander, R., & Bodnar, R. (2010). A 48 my history of fracture opening, temperature, and fluid pressure: Cretaceous Travis Peak Formation, East Texas basin. *Bulletin*, 122(7-8), 1081–1093.
- Bello, R. O., Wattenbarger, R. A., et al. (2010). Multi-stage hydraulically fractured horizontal shale gas well rate transient analysis. In *North africa technical conference and exhibition*.
- Berkowitz, B. (1995). Analysis of fracture network connectivity using percolation theory. *Mathematical Geology*, 27(4), 467–483. doi: 10.1007/BF02084422
- Berkowitz, B. (2002). Characterizing flow and transport in fractured geological media: A review. *Advances in Water Resources*, 25(8-12), 861–884.
- Berkowitz, B., Bour, O., Davy, P., & Odling, N. (2000). Scaling of fracture connectivity in geological formations. *Geophysical Research Letters*, 27(14), 2061–2064.
- Biot, M. A. (1941). General theory of three-dimensional consolidation. *Journal of applied physics*, 12(2), 155–164.
- Bonnet, E., Bour, O., Odling, N. E., Davy, P., Main, I., Cowie, P., & Berkowitz, B. (2001). Scaling of fracture systems in geological media. *Reviews of geophysics*, 39(3), 347–383.
- Bour, O., & Davy, P. (1997). Connectivity of random fault networks following a power law fault length distribution. *Water Resources Research*, 33(7), 1567–1583.
- Budai, J., Martini, A., Walter, L., & Ku, T. (2002). Fracture-fill calcite as a record of microbial methanogenesis and fluid migration: a case study from the Devonian Antrim Shale, Michigan Basin. *Geofluids*, 2(3), 163–183.
- Cook, A., Myer, L., Cook, N., & Doyle, F. (1990). The effects of tortuosity on flow through a natural fracture.
- Coulomb, C. (1773). Essai sur une application des regles de maximis et minimis a quelques problemes de statique relatifs a l’architecture. *Mem. Div. Sav. Acad.*
- Das, I., & Zoback, M. D. (2013). Long-period, long-duration seismic events during hydraulic stimulation of shale and tight-gas reservoirs—Part 1: Waveform characteristicsLPLD events: Waveform characteristics. *Geophysics*, 78(6), KS107–KS118.
- Engelder, T., Gross, M., & Pinkerton, P. (1997). Joint development in clastic rocks of the elk basin anticline, montana-wyoming: An analysis of fracture spacing versus bed thickness in a basement-involved laramide structure. *Fractured reservoirs: Characterization and modeling: Rocky Mountain Association of Geologists*, 1–18.

- Evans, K. F. (2005). Permeability creation and damage due to massive fluid injections into granite at 3.5 km at Soultz: 2. Critical stress and fracture strength. *Journal of Geophysical Research: Solid Earth*, 110(B4).
- Fisher, M., Heinze, J., Harris, C., Davidson, B., Wright, C., Dunn, K., et al. (2004). Optimizing horizontal completion techniques in the Barnett shale using microseismic fracture mapping. In *Spe annual technical conference and exhibition*.
- Fisher, M. K., Wright, C. A., Davidson, B. M., Goodwin, A., Fielder, E., Buckler, W., ... others (2002). Integrating fracture mapping technologies to optimize stimulations in the Barnett Shale. In *Spe annual technical conference and exhibition*.
- Frash, L. P., Carey, J. W., & Welch, N. J. (2019). Scalable en echelon shear-fracture aperture-roughness mechanism: Theory, validation, and implications. *Journal of Geophysical Research: Solid Earth*, 124(1), 957–977.
- Gross, M. R. (1993). The origin and spacing of cross joints: examples from the Monterey Formation, Santa Barbara Coastline, California. *Journal of Structural Geology*, 15(6), 737–751.
- Holland, M., & Urai, J. L. (2010). Evolution of anastomosing crack–seal vein networks in limestones: Insight from an exhumed high-pressure cell, Jabal Shams, Oman Mountains. *Journal of Structural Geology*, 32(9), 1279–1290.
- Huang, Q., & Angelier, J. (1989). Fracture spacing and its relation to bed thickness. *Geological Magazine*, 126(4), 355–362.
- Hubbert, M. K., et al. (1956). Darcy’s law and the field equations of the flow of underground fluids. *Transactions of the AIME*, 207(01), 222–239.
- Hubbert, M. K., & Willis, D. G. (1972). Mechanics of hydraulic fracturing.
- Im, K., Elsworth, D., & Fang, Y. (2018). The influence of preslip sealing on the permeability evolution of fractures and faults. *Geophysical Research Letters*, 45(1), 166–175.
- Ito, T., & Hayashi, K. (2003). Role of stress-controlled flow pathways in HDR geothermal reservoirs. *Pure and applied geophysics*, 160(5-6), 1103–1124.
- Ito, T., & Zoback, M. D. (2000). Fracture permeability and in situ stress to 7 km depth in the KTB scientific drillhole. *Geophysical Research Letters*, 27(7), 1045–1048.
- Karimi-Fard, M., Durlofsky, L. J., Aziz, K., et al. (2003). An efficient discrete fracture model applicable for general purpose reservoir simulators. In *Spe reservoir simulation symposium*.
- Kim, H., & Inoue, J. (2003). Analytical approach for anisotropic permeability through a single rough rock joint under shear deformation. *Journal of Geophysical Research: Solid Earth*, 108(B8).
- Lander, R., & Laubach, S. (2015). Insights into rates of fracture growth and sealing from a model for quartz cementation in fractured sandstones. *Bulletin*, 127(3-4), 516–538.
- Laubach, S., Lander, R., Bonnell, L., Olson, J., & Reed, R. (2004). Opening histories of fractures in sandstone. *Geological Society, London, Special Publications*, 231(1), 1–9.
- Laubach, S., Reed, R., Olson, J., Lander, R., & Bonnell, L. (2004). Coevolution of crack-seal texture and fracture porosity in sedimentary rocks: cathodoluminescence observations of regional fractures. *Journal of Structural Geology*, 26(5), 967–982.
- Laubach, S. E. (2003). Practical approaches to identifying sealed and open fractures. *AAPG bulletin*, 87(4), 561–579.
- Laubach, S. E., & Ward, M. E. (2006). Diagenesis in porosity evolution of opening-mode fractures, middle triassic to lower jurassic la boca formation, ne mexico. *Tectonophysics*, 419(1-4), 75–97.
- Lee, Y.-J., & Morse, J. W. (1999). Calcite precipitation in synthetic veins: implications for the time and fluid volume necessary for vein filling. *Chemical Geology*, 156(1-4), 151–170.
- Lei, Q., Latham, J.-P., & Tsang, C.-F. (2017). The use of discrete fracture networks for modelling coupled geomechanical and hydrological behaviour of fractured rocks. *Computers and Geotechnics*, 85, 151–176.
- Maghsoudi, S., Eaton, D. W., & Davidsen, J. (2016). Nontrivial clustering of microseismicity induced by hydraulic fracturing. *Geophysical Research Letters*, 43(20), 10–672.

- Marder, M., Chen, C.-H., & Patzek, T. (2015). Simple models of the hydrofracture process. *Physical Review E*, *92*(6), 062408.
- Masihi, M., King, P. R., Nurafza, P. R., et al. (2007). Fast estimation of connectivity in fractured reservoirs using percolation theory. *SPE Journal*, *12*(02), 167–178.
- Mattila, J., & Follin, S. (2019). Does In Situ State of Stress Affect Fracture Flow in Crystalline Settings? *Journal of Geophysical Research: Solid Earth*, *124*(5), 5241–5253.
- Mayerhofer, M. J., Lolon, E., Warpinski, N. R., Cipolla, C. L., Walser, D. W., Rightmire, C. M., et al. (2010). What is stimulated reservoir volume? *SPE Production & Operations*, *25*(01), 89–98.
- Mayerhofer, M. J., Lolon, E. P., Youngblood, J. E., Heinze, J. R., et al. (2006). Integration of microseismic-fracture-mapping results with numerical fracture network production modeling in the Barnett Shale. In *Spe annual technical conference and exhibition*.
- Mo, H., Bai, M., Lin, D., & Roegiers, J.-C. (1998). Study of flow and transport in fracture network using percolation theory. *Applied Mathematical Modelling*, *22*(4-5), 277–291.
- Morrow, C., Moore, D. E., & Lockner, D. (2000). The effect of mineral bond strength and adsorbed water on fault gouge frictional strength. *Geophysical research letters*, *27*(6), 815–818.
- Muralidharan, V., Chakravarthy, D., Putra, E., Schechter, D., et al. (2004). Investigating fracture aperture distributions under various stress conditions using x-ray ct scanner. In *Canadian international petroleum conference*.
- Narr, W., & Suppe, J. (1991). Joint spacing in sedimentary rocks. *Journal of Structural Geology*, *13*(9), 1037–1048.
- Newman, M. E., & Ziff, R. M. (2001). Fast Monte Carlo algorithm for site or bond percolation. *Physical Review E*, *64*(1), 016706.
- Nomura, T., Tabuchi, K., Zhu, C., Sheng, N., Wang, S., & Akiyama, T. (2015). High thermal conductivity phase change composite with percolating carbon fiber network. *Applied energy*, *154*, 678–685.
- Olson, J. E. (2003). Sublinear scaling of fracture aperture versus length: an exception or the rule? *Journal of Geophysical Research: Solid Earth*, *108*(B9).
- Rateman, K. T., Farrell, H. E., Mora, O. S., Janssen, A. L., Gomez, G. A., Busetti, S., ... others (2018). Sampling a stimulated rock volume: An eagle ford example. *SPE Reservoir Evaluation & Engineering*, *21*(04), 927–941.
- Rawnsley, K., Rives, T., Petti, J.-P., Hencher, S., & Lumsden, A. (1992). Joint development in perturbed stress fields near faults. *Journal of Structural Geology*, *14*(8-9), 939–951.
- Renshaw, C. E. (1995). On the relationship between mechanical and hydraulic apertures in rough-walled fractures. *Journal of Geophysical Research: Solid Earth*, *100*(B12), 24629–24636.
- Renshaw, C. E., Schulson, E. M., Iliescu, D., & Murzda, A. (2020). Increased fractured rock permeability after percolation despite limited crack growth. *Journal of Geophysical Research: Solid Earth*, *125*(8), e2019JB019240.
- Robinson, P. (1983). Connectivity of fracture systems-a percolation theory approach. *Journal of Physics A: Mathematical and General*, *16*(3), 605.
- Ruf, J. C., Rust, K. A., & Engelder, T. (1998). Investigating the effect of mechanical discontinuities on joint spacing. *Tectonophysics*, *295*(1-2), 245–257.
- Sandve, T. H., Berre, I., & Nordbotten, J. M. (2012). An efficient multi-point flux approximation method for discrete fracture-matrix simulations. *Journal of Computational Physics*, *231*(9), 3784–3800.
- Sen, Z., & Kazi, A. (1984). Discontinuity spacing and RQD estimates from finite length scanlines. In *International journal of rock mechanics and mining sciences & geomechanics abstracts* (Vol. 21, pp. 203–212).
- Shaffner, J. T., Cheng, A., Simms, S., Keyser, E., Yu, M., et al. (2011). The advantage of incorporating microseismic data into fracture models. In *Canadian unconventional resources conference*.
- Snow, D. T. (1970). The frequency and apertures of fractures in rock. In *International*

- 779 *journal of rock mechanics and mining sciences & geomechanics abstracts* (Vol. 7, pp.  
780 23–40).
- 781 Stauffer, D., & Aharony, A. (1994). *Introduction To Percolation Theory*. CRC Press.
- 782 Syed Haider, S. W., & W., P. T. (2020). The key physical factors that yield a good  
783 horizontal hydrofractured gas well in mudrock. *Energies*, 13(9), 2348. doi: doi.org/  
784 10.3390/en13092348
- 785 Thomas, R. N., Paluszny, A., & Zimmerman, R. W. (2017). Quantification of fracture inter-  
786 action using stress intensity factor variation maps. *Journal of Geophysical Research:  
787 Solid Earth*, 122(10), 7698–7717.
- 788 Ukar, E., & Laubach, S. E. (2016). Syn-and postkinematic cement textures in fractured car-  
789 bonate rocks: Insights from advanced cathodoluminescence imaging. *Tectonophysics*,  
790 690, 190–205.
- 791 Warpinski, N. R., Mayerhofer, M., Agarwal, K., Du, J., et al. (2013). Hydraulic-fracture  
792 geomechanics and microseismic-source mechanisms. *SPE Journal*, 18(04), 766–780.
- 793 Warpinski, N. R., Mayerhofer, M. J., Vincent, M. C., Cipolla, C. L., Lonon, E., et al. (2009).  
794 Stimulating unconventional reservoirs: maximizing network growth while optimizing  
795 fracture conductivity. *Journal of Canadian Petroleum Technology*, 48(10), 39–51.
- 796 Warpinski, N. R., Wolhart, S., Wright, C., et al. (2001). Analysis and prediction of mi-  
797 croseismicity induced by hydraulic fracturing. In *Spe annual technical conference and  
798 exhibition*.
- 799 Watkins, H., Bond, C. E., Healy, D., & Butler, R. W. (2015). Appraisal of fracture  
800 sampling methods and a new workflow to characterise heterogeneous fracture networks  
801 at outcrop. *Journal of Structural Geology*, 72, 67–82.
- 802 Wenning, Q. C., Madonna, C., Kurotori, T., & Pini, R. (2019). Spatial mapping of frac-  
803 ture aperture changes with shear displacement using X-ray computerized tomography.  
804 *Journal of Geophysical Research: Solid Earth*, 124, 7320–7340.
- 805 Westergaard, H. M. (1939). Bearing pressures and cracks. *Trans AIME, J. Appl. Mech.*, 6,  
806 49–53.
- 807 Xie, L., & Min, K.-B. (2016). Initiation and propagation of fracture shearing during hy-  
808 draulic stimulation in enhanced geothermal system. *Geothermics*, 59, 107–120.
- 809 Yeo, I., De Freitas, M., & Zimmerman, R. (1998). Effect of shear displacement on the  
810 aperture and permeability of a rock fracture. *International Journal of Rock Mechanics  
811 and Mining Sciences*, 35(8), 1051–1070.
- 812 Zhu, W., He, X., & Patzek, T. W. (2021). Insights into the coupled effects of fracture  
813 geometry and sealing on stimulated reservoir volume in shales. In *3rd international  
814 discrete fracture network engineering conference*.
- 815 Zhu, W., Khirevich, S., & Patzek, T. (2018). Percolation properties of stochastic fracture  
816 networks in 2D and outcrop fracture maps. In *80th eage conference and exhibition  
817 2018* (Vol. 2018, pp. 1–5).
- 818 Zhu, W., Khirevich, S., & Patzek, T. (2020). Fracture recognition with u-net and pixel-  
819 based automatic fracture detection. In *Fourth naturally fractured reservoir workshop  
820* (Vol. 2020, pp. 1–5).
- 821 Zhu, W., Khirevich, S., & Patzek, T. W. (2021). Impact of fracture geometry and topol-  
822 ogy on the connectivity and flow properties of stochastic fracture networks. *Water  
823 Resources Research*, 57(7), e2020WR028652.
- 824 Zhu, W., Yalcin, B., Khirevich, S., & Patzek, T. (2019). Correlation Analysis of Fracture  
825 Intensity Descriptors with Different Dimensionality in a Geomechanics-constrained 3D  
826 Fracture Network. In *Petroleum geostatistics 2019* (Vol. 2019, pp. 1–5).
- 827 Zimmerman, R., Kumar, S., & Bodvarsson, G. (1991). Lubrication theory analysis of the  
828 permeability of rough-walled fractures. In *International journal of rock mechanics and  
829 mining sciences & geomechanics abstracts* (Vol. 28, pp. 325–331).
- 830 Zimmerman, R. W., & Bodvarsson, G. S. (1996). Hydraulic conductivity of rock fractures.  
831 *Transport in porous media*, 23(1), 1–30.
- 832 Zoback, M. D., & Gorelick, S. M. (2012). Earthquake triggering and large-scale geologic  
833 storage of carbon dioxide. *Proceedings of the National Academy of Sciences*, 109(26),

